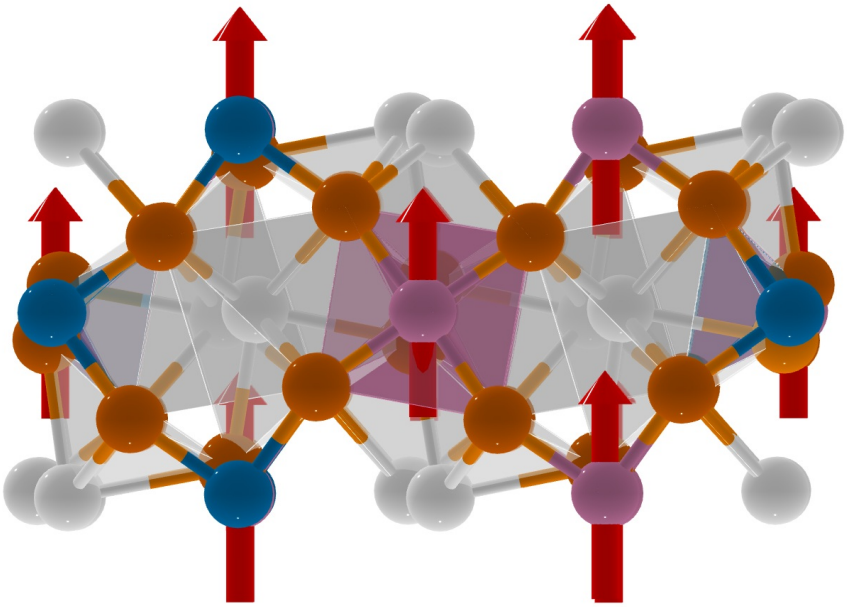

Neural Networks in Materials Exploration

Computational Thermodynamic Screening of Doped $CaMnO_3$ with Oxygen Vacancies for Chemical Looping Combustion

Master's thesis in Space, earth and environment

Alfred Juhlin Onbeck

DEPARTMENT OF SPACE, EARTH AND ENVIRONMENT

CHALMERS UNIVERSITY OF TECHNOLOGY
Gothenburg, Sweden 2025
www.chalmers.se

Master's thesis 2025

Neural Networks in Materials Exploration

Computational Thermodynamic Screening of Doped $CaMnO_3$ with Oxygen Vacancies for Chemical Looping Combustion

Alfred Juhlin Onbeck

CHALMERS
UNIVERSITY OF TECHNOLOGY

Department of Space, Earth and Environment
Division of Energy Technology
Chalmers University of Technology
Gothenburg, Sweden 2025

Neural Networks in Materials Exploration
Computational Thermodynamic Screening of Doped $CaMnO_3$ with Oxygen Vacancies for Chemical Looping Combustion
Alfred Juhlin Onbeck

Supervisor: Jonatan Gastaldi, Department of Space, Earth and Environment
Examiner: Tobias Mattison, Department of Space, Earth and Environment

Master's Thesis 2025
Department of Space, Earth and Environment
Division of Energy Technology
Chalmers University of Technology
SE-412 96 Gothenburg
Telephone +46 31 772 1000

Cover: $Ca_4Mn_3TiO_{12}$ taken from Materials Project Database.

Printed by Chalmers Reproservice
Gothenburg, Sweden 2025

Neural Networks in Materials Exploration
Computational Thermodynamic Screening of Doped $CaMnO_3$ with Oxygen Vacancies for Chemical Looping Combustion
Alfred Juhlin Onbeck
Department of Space, Earth and Environment
Chalmers University of Technology

Abstract

To support the development of efficient CO_2 capture technologies, we computationally evaluate the thermodynamic behavior of doped $CaMnO_3$ with oxygen vacancies for chemical looping combustion (CLC). The approach combines a machine learning interatomic potential (CHGNet) for efficient near first-principles-level atomistic modeling, the cluster expansion (CE) technique to determine ground-state configurations, phonon calculations for vibrational contributions to heat capacity, and Monte Carlo simulations to capture configurational entropy.
Doping was performed on the B-site with Ti, Fe, Si, Cr, Cu, Mo, and Mg, and on the A-site with Ce, Sr, La, and Bi, at concentrations ranging from 1/16 to 6/16. A screening using the Bartel tolerance factor was conducted across the periodic table to identify dopants with favorable perovskite stability. Thermodynamic phase diagram analysis revealed promising oxygen carrier behavior for Ce- and Sr-doping on the A-site, and Fe- and Ti-doping on the B-site. Among these dopants, Ce and Ti significantly enhanced the overall thermodynamic stability of the oxide, while Fe and Sr promoted oxygen vacancy formation at lower temperatures and higher oxygen partial pressures, albeit with slightly reduced stability compared to Ce and Ti.
These results highlight the thermodynamic tunability of $CaMnO_3$-based perovskites through strategic doping, providing insight for the design of stable oxygen carriers for CLC applications.

Keywords: Thermodynamic properties, phase equilibrium, CLC, Doped $CaMnO_3$

Acknowledgements

I would like to sincerely thank my supervisor, Jonatan Gastaldi, for their guidance, support, and encouragement throughout this project. I am also grateful to my examiner, Tobias Mattisson, for their constructive feedback and thoughtful evaluation. Finally, I would like to thank Anders Hellman for helpful discussions and valuable input that contributed to the development of this work.

Alfred Juhlin Onbeck, Gothenburg, July 2025

List of Acronyms

Below is the list of acronyms that have been used throughout this thesis listed in alphabetical order:

ARDR	Automatic Relevance Determination Regression
BECCS	Bioenergy with Carbon Capture and Storage
CCS	Carbon Capture and Storage
CE	Cluster Expansion
CHGNet	Charge Graph Neural Network
CLC	Chemical Looping Combustion
CN	Coordination Number
DFT	Density Functional Theory
DOS	Density of States
ECIs	Effective Cluster Interactions
MC	Monte Carlo
MLP	Machine Learning Potential
OC	Oxygen Carrier

Nomenclature

Below is the nomenclature of parameters, and variables that have been used throughout this thesis.

Thermodynamics

H	Enthalpy
E	Internal energy (2.4) or potential energy (2.5)
S	Entropy
C_V	Heat capacity at constant volume
C_p	Heat capacity at constant pressure
R	Chemical reaction (subscript)
f	Formation (subscript), e.g., $\Delta_f H$ formation enthalpy
T	Temperature
p_{O_2}	Oxygen partial pressure
V	Volume
k_B	Boltzmann constant

Miscellaneous

P	Probability
p	Probability, Boltzmann distribution
N_i	Number of atoms of specie i
r_X	Ionic radius of X-site ion
r_O	Ionic radius of O^{2-}
r_A	Ionic radius of A-site ion
r_B	Ionic radius of B-site ion
n_A	Oxidation state of A-site ion

τ	Bartel tolerance factor
σ	Standard deviation
α	(Method) Regularization parameter for ridge regression
x	Generally doping concentration, occasionally stoichometric oxygen vacancies (integer)
δ	Non-stoichiometric oxygen vacancies ($0 \leq \delta \leq 0.5$)
F_β	Force on atom, β direction (x,y,z)
$\Phi_{\alpha\beta}$	Force constant tensor
$\mathbf{q}$	Wave vector
ω	Phonon frequency
$\boldsymbol{Q}$	Property vector, e.g., total energy
$\mathbf{\Pi}$	Matrix, stacked set of cluster vectors
$\boldsymbol{J}$	Vector of effective cluster interactions

Indices

α	(Theory) Direction x, y, or z
β	Direction x, y, or z
j	Atom j or phonon branch j
j'	Atom j'
l	Unit cell l
l'	Unit cell l'

Contents

List of Figures

List of Tables

1
Introduction

1.1 Climate Change and CO_2 Emissions

There is strong scientific consensus that global warming is primarily driven by human activities, particularly through the emission of greenhouse gases such as carbon dioxide (CO_2) [1]. CO_2 is the single largest contributor to climate change, largely originating from the combustion of fossil fuels and biomass for energy production. One of the most promising strategies to mitigate CO_2 emissions is carbon capture and storage (CCS) [1]. When CCS is applied to biomass combustion, a process known as bioenergy with carbon capture and storage (BECCS), it can even achieve negative emissions, effectively removing CO_2 from the atmosphere [2]. However, fossil fuels remain the dominant source of global CO_2 emissions, accounting for approximately 80% [3].

1.2 Chemical Looping Combustion

Chemical looping combustion (CLC) is an emerging CCS-compatible technology that offers a promising high-efficiency alternative to other CCS technologies where energy-intensive gas separation is required [4]. In CLC, metal oxides are used as oxygen carriers (OCs) to transfer oxygen from air to fuel through a reduction-oxidation (redox) cycle. As the fuel is oxidized without direct contact with air, the resulting flue gas consists primarily of CO_2 and H_2O in concentrated form. This enables straightforward CO_2 capture by simple condensation of water vapor, eliminating the need for energy-intensive gas separation steps and thereby improving overall efficiency [5].

The performance of a CLC system is closely tied to the properties of its oxygen carriers. Key requirements include high redox activity, thermal and chemical stability, fast oxygen release and uptake, and resistance to sintering and attrition over repeated cycles. A critical challenge is maintaining these properties over long-term operation, especially under high-temperature conditions [5].

In the past two decades, there have been a significant number of studies related to the development of oxygen carrier materials with more than 900 OCs tested [5]. Most of the oxygen carriers which have been studied are based on the transition metals Fe, Mn, Cu and Ni with a pure phase transition, e.g. $Fe_2O_3 \rightarrow Fe_3O_4$ [6].

Among these candidates, perovskite oxides have emerged as particularly promising due to their tunable crystal structure and excellent redox behavior while also avoiding pure phase transitions [7]. Systematic doping at both the A- and B-sites

of perovskite structures such as $CaMnO_3$ enables the identification of compositions with enhanced thermodynamic stability and redox performance, positioning them as strong contenders for durable and efficient OCs for use in CLC [8].

1.3 Perovskite Oxides as Oxygen Carriers

Perovskite oxides show great potential as oxygen carriers because of their tunability through doping and chemical stability [9]. These oxides, with the general formula ABO_3, typically consists of a rare earth or alkaline earth metal with large atomic radius at the A-site and a transition metal with small atomic radius at the B-site. By doping at the A- and B-sites, the physical and chemical properties of the oxygen carrier can be improved. Doping at the A-site primarily influences oxygen vacancy formation and ionic transport, while doping at the B site affects redox behavior and catalytic activity [10].
Among perovskite oxides, $CaMnO_3$-based perovskites are particularly attractive due to their low cost, calcium and manganese are relatively inexpensive, as well as their high reactivity and strong oxygen uncoupling ability [11]. These properties make them ideal candidates for use in CLC, where fast and reversible oxygen exchange is essential. However, thermodynamic data of $CaMnO_3$ remains limited, despite its importance for improving efficiency and optimization of the system. In particular, discrepancies between experimental observations and computational studies have been reported for pristine $CaMnO_3$, highlighting the need for further investigation [12].

1.4 Objectives and Limitations

In this work, the goal is to perform a systematic screening of various dopants at the A- and B-sites of $CaMnO_3$ to evaluate their influence on key thermodynamic properties, such as formation enthalpy and Gibbs free energy. These properties are essential for assessing phase stability and predicting the behavior of doped compounds under realistic conditions. Furthermore, the formation energy of oxygen vacancies is examined to determine how readily oxygen can be released and reincorporated during redox cycling. This work utilizes a computational approach based indirectly on first-principles data and density functional theory (DFT) to estimate thermodynamic properties. However, in order to speed up calculations and allow larger supercells, a Machine Learning Potential (MLP, specifically CHGNet) was employed and is fundamental to the methodology. This general screening approach aims to identify promising dopant candidates that enhance the stability of $CaMnO_3$-based materials as oxygen carriers in CLC systems.
The primary limitations of this work, due to constraints in time and computational resources, are the restricted set of dopants considered and the exclusive focus on the orthorhombic perovskite structure. Dopants were generally selected based on their perceived promise, as identified in the limited number of existing studies on doped $CaMnO_3$. The orthorhombic phase was chosen because of its greater thermodynamic stability at intermediate temperatures (25 °C to 800 °C) compared to

the cubic phase for pristine $CaMnO_3$ [13]. Additional limitations include the discrete doping concentrations investigated (1/16, 2/16, ..., 6/16) and the range of non-stoichiometric oxygen vacancy concentrations considered (1/48, ..., 8/48).

2

Background

2.1 Chemical Looping Combustion (CLC)

Chemical looping combustion is a promising energy conversion technology that enables intrinsic separation of carbon dioxide while maintaining high efficiency. It operates by splitting the combustion process into two interconnected steps using a solid oxygen carrier, thereby avoiding direct contact between air and fuel, see Figure 2.1 [14].

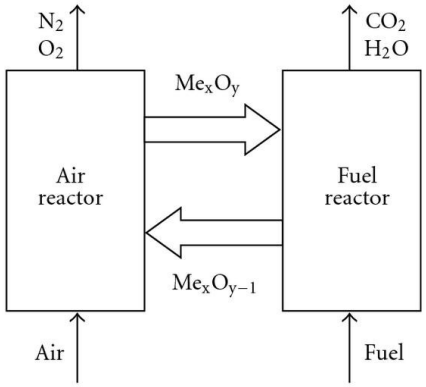

Figure 2.1: Schematic representation of the chemical looping combustion (CLC) process. The system consists of two reactors: an air reactor, where the metal (Me_xO_{y-1}) is oxidized by air, and a fuel reactor, where the oxidized metal (Me_xO_y) reacts with the fuel to release energy and produce CO_2 and H_2O. The metal oxide circulates between the two reactors, enabling indirect combustion without direct mixing of air and fuel. Taken from [15].

In a typical CLC system two fluidized bed reactors are employed: an air reactor and a fuel reactor. In the air reactor, the oxygen carrier, typically a metal oxide, is oxidized by air [5]:

$$Me_xO_{y-1} + \frac{1}{2}O_2 \rightarrow Me_xO_y. \tag{2.1}$$

The oxidized carrier is then transported to the fuel reactor, where it transfers lattice oxygen to the fuel (e.g., methane) and is reduced in the process (non-hydrocarbons may have other flue gasses) [5]:

$$Me_xO_y + \text{Fuel} \rightarrow Me_xO_{y-1} + CO_2 + H_2O \tag{2.2}$$

Since the fuel does not come into contact atmospheric nitrogen, the exhaust from the fuel reactor contains mainly CO_2 and H_2O, allowing for efficient CO_2 capture via condensation of water vapor. The reduced carrier is cycled back to the air reactor to repeat the process [5].
CLC is particularly attractive for integration with industrial combustion and power generation processes, as it offers a path toward low-emission energy systems without the efficiency penalties associated with traditional carbon capture technologies [16].

2.2 Computational Background

The computational part of the methodology can be split into four main parts.

1. The machine learning potential **CHGNet** serves as the core computational "calculator" throughout the methodology. It is used to predict energies and atomic forces, and to perform structure relaxations by minimizing forces to locate local minima on the potential energy surface.
2. **Cluster expansion (CE)** is employed primarily to identify ground-state configurations of doped $CaMnO_3$ compounds. In addition, it is also used in later stages for computing both phononic and configurational heat capacities. CE is applied only to doped $CaMnO_3$, not to the binary metal oxides used as references. It is specifically used for systems with mixed occupancies (i.e. partial substitution or oxygen vacancy disorder), where configurational degrees of freedom significantly influence thermodynamic properties.
3. **Phononic heat capacity** is a critical component in the computational determination of thermodynamic properties, as it directly contributes to the calculation of the reaction heat capacity. A detailed description of the thermodynamic theory is provided in the following chapter.
4. **Configurational heat capacity** is also crucial, as doping introduces configurational degrees of freedom in $CaMnO_3$, resulting in configurational entropy. This heat capacity contribution is included in the calculation of reaction heat capacity, but only relevant mixed materials such as doped $CaMnO_3$.

2.2.1 CHGNet

CHGNet (Charge Graph Neural Network) [17] is a machine learning interatomic potential designed to approximate the accuracy of DFT while allowing larger-scale atomistic simulations. It is trained on static calculations and relaxation trajectories of ~ 1.37 million structures from the Materials Project Database, covering the entire periodic table. By predicting total energies, forces, and charges directly from atomic configurations, CHGNet provides near-DFT accuracy at a fraction of the computational cost.
Compared to DFT, which solves the Kohn–Sham equations self-consistently for each structure, CHGNet eliminates the need for iterative electronic structure calculations. This results in speedups of several orders of magnitude, making it feasible to explore large configurational and temperature-dependent spaces that are computationally prohibitive with DFT. However, CHGNet inherits the limitations of its training data and may underperform for structures outside its training set.

2.2.2 Cluster Expansion

The cluster expansion formalism offers a systematic and efficient approach for modeling the configurational dependence of properties—e.g., the total energy—in crystalline solids. Initially developed for alloy thermodynamics, CE has since been extended to treat multicomponent systems, ionic compounds, as well as materials containing vacancies [18]. For binary metal oxides, ground-state structures are typically available from the Materials Project database. However, for mixed metal oxides, such as doped $CaMnO_3$, the ground state is typically not available. In these cases, CE is employed to predict the lowest-energy structure across the configurational space. Note that the pristine ground state structure of $CaMnO_3$ is available and is used as the basis for constructing the training set.
In the CE formalism, a crystalline lattice is represented as a set of fixed sites, each of which can be occupied by different atomic species or states (e.g., vacancies). A configuration refers to a specific occupation pattern across these sites. The property of interest, typically the total energy Q_i, is then expressed as an expansion over clusters of interacting sites

$$\boldsymbol{Q} = \boldsymbol{\Pi} \boldsymbol{J}, \tag{2.3}$$

where $\boldsymbol{\Pi}$ is the design matrix, with each row representing a configuration and each column corresponding to a distinct cluster function. The vector $\boldsymbol{J}$ contains the effective cluster interactions (ECIs) for various cluster types (see Figure 2.2). The expansion is truncated using symmetry and distance-based cutoffs, retaining only the most relevant groups of symmetrically equivalent clusters, known as orbits.

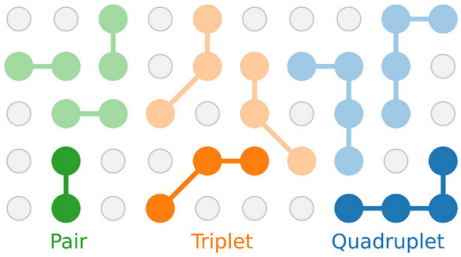

Figure 2.2: Visual example of different ordered clusters: pairs, triplets and quadruplets. Taken from [18].

The strength of the CE approach lies in its ability to efficiently represent long-range interactions using a compact set of terms. The ECIs are specific to the system and must be learned by fitting to a training set of configurations with known energies. These reference energies are typically obtained from first-principles methods such as density functional theory (DFT), or as in this work employs a more computationally efficient machine learning potential (MLP), specifically CHGNet, which will be discussed in the following section.
Although MLPs are significantly more efficient than DFT, exhaustively evaluating the full configuration space remains computationally prohibitive due to the exponential growth in the number of distinct configurations with increasing system size and complexity. The CE method circumvents this by enabling the extrapolation of

configurational energies from a limited set of reference calculations, thereby allowing efficient identification of the ground-state structure among a vast space of possible configurations.

2.2.3 Phononic Heat Capacity

Lattice vibrations in crystalline solids can be described using phonons, which are quantized vibrational modes of the atomic lattice. Under the harmonic approximation, the potential energy of the system is expanded up to second order in atomic displacements. The coefficients of this expansion are the *second-order force constants*, which quantify how the force on one atom changes due to the displacement of another atom.
The second-order force constant tensor $\Phi_{\alpha\beta}(jl, j'l')$, which corresponds to the second derivative of the potential energy, describes the force in the Cartesian direction β on atom j' in unit cell l' resulting from a displacement in direction α of atom j in unit cell l. These force constants are typically computed using the finite displacement method [19]:

$$\Phi_{\alpha\beta}(jl, j'l') \simeq -\frac{F_\beta(j'l'; \Delta r_\alpha(jl)) - F_\beta(j'l')}{\Delta r_\alpha(jl)}, \tag{2.4}$$

where $F_\beta(j'l'; \Delta r_\alpha(jl))$ is the force on the atom j' in direction β after a small displacement Δr_α of atom j, and usually $F_\beta(j'l') \equiv 0$ for a relaxed configuration.
Once the force constants are known, they can be used to compute the phonon frequencies $\omega_{\mathbf{q}j}$. These frequencies determine the vibrational contribution to the internal energy of the crystal at temperature T

$$E(T) = \sum_{\mathbf{q},j} \left[\frac{1}{2}\hbar\omega_{\mathbf{q}j} + \frac{\hbar\omega_{\mathbf{q}j}}{e^{\hbar\omega_{\mathbf{q}j}/k_B T} - 1} \right]. \tag{2.5}$$

The constant volume heat capacity C_V is then obtained by differentiating the internal energy with respect to temperature.

$$C_V(T) = \left(\frac{\partial E}{\partial T}\right)_V = k_B \sum_{\mathbf{q},j} \left(\frac{\hbar\omega_{\mathbf{q}j}}{k_B T}\right)^2 \frac{e^{\hbar\omega_{\mathbf{q}j}/k_B T}}{\left(e^{\hbar\omega_{\mathbf{q}j}/k_B T} - 1\right)^2}. \tag{2.6}$$

2.2.4 Configurational Heat Capacity

The configurational heat capacity arises from fluctuations in the potential energy of a system at fixed composition and temperature. In the canonical ensemble ($N_i VT$), the number of atoms of each species (N_i), volume (V), and temperature (T) are held constant. The probability of the system occupying a particular configuration is governed by the Boltzmann distribution [18]:

$$p_{\mathrm{C}} \propto \exp\left(-\frac{E}{k_B T}\right), \tag{2.7}$$

where E is the potential energy of the configuration and k_B is the Boltzmann constant.

This concept is relevant only for systems with configurational degrees of freedom, such as doped or oxygen-deficient $CaMnO_3$, where two or more atomic species occupy the same sublattice and can be exchanged. These site occupations contribute to the entropy of the system and therefore to a temperature-dependent configurational heat capacity.
To evaluate this contribution, Monte Carlo simulations are typically used to sample the configurational space while maintaining a fixed composition. The trial steps involve swapping the identities of two dissimilar atoms to preserve stoichiometry. Each swap is accepted with the probability:

$$P = \min\left\{1, \exp\left(-\frac{\Delta E}{k_B T}\right)\right\}, \tag{2.8}$$

where ΔE is the energy change that results from the proposed swap.
Over the course of a Monte Carlo simulation, the variance σ^2 of the potential energy distribution can be used to compute the configurational heat capacity at a constant volume:

$$C_V^{\text{conf}} = \frac{\sigma^2}{k_B T^2}. \tag{2.9}$$

The total constant-volume heat capacity for the doped structure is then obtained by summing the configurational and phononic contributions:

$$C_V = C_V^{\text{phonon}} + C_V^{\text{conf}}. \tag{2.10}$$

For the other compounds in the "reaction", the heat capacity consists purely of the phononic contribution. Here, "reaction" refers to the chemical balance used to incorporate reference metal oxides and experimental data; this is discussed in more detail in the next chapter.

3
Methods

The methodology for evaluating the formation enthalpy and other thermodynamic properties of mixed metal oxides in this project follows the procedure developed by Brorsson *et al.* [20, 12], which is itself based on the earlier work of Benisek & Dachs [21].

3.1 Methodology Outline

The first step in the methodology, as illustrated in Figure 3.1, involves identifying the chemical reaction of interest and the associated compounds. A fundamental aspect of this approach is the use of binary metal oxides as "reference" structures to serve as corrections for the more complex mixed metal oxide product, as described further in Section 3.3. Binary oxides are selected due to their abundance of experimental data and their chemical similarity to the target compound. In cases where sufficient experimental data are not available to balance the reaction, oxygen is added to ensure stoichiometric balance; this adjustment is necessary for elements such as La, Bi, and Mg. Ground state structures are primarily sourced from the Materials Project database [22], with the exception of materials containing mixed site occupancies (i.e., doped structures).

For compounds not directly available in the Materials Project (such as doped or structures with oxygen vacancies), the ground state configurations must be determined computationally. This is achieved by generating a sample of representative configurations based of the pristine ground state using the `ICET` [18] package to be used for cluster expansion training. The pristine ground state of $CaMnO_3$ was only considered in the orthorhombic perovskite structure due to its higher stability from room temperature up to 800 °C [13].

Once the training structures are generated, they are relaxed using the CHGNet [17] machine learning potential to reach local energy minima, after which the relaxed structures are used to construct a cluster expansion model. This model is then optimized to identify the ground state configuration of the system, from which reaction enthalpies at 0 K are calculated, as presented in Section 3.3.

To account for vibrational contributions, harmonic force constants are computed using the `HiPhive` [23] package. Phonon properties, including the harmonic heat capacity, are subsequently obtained through the use of the `Phonopy` package [24, 19]. For systems with dopant elements or mixed occupancy, the configurational heat capacity is evaluated using Monte Carlo simulations. These simulations are performed using the `mchammer` module within the `ICET` package.

Finally, experimental thermochemical data for binary metal oxides, sourced from the NIST-JANAF thermochemical tables, are employed to adjust the calculated values of heat capacity, entropy, and formation enthalpy. In cases where a metal oxide was unavailable in the NIST-JANAF tables, data was retrieved from a FactSage database (FToxid) as an alternative [25]. Specifically, Bi_2O_3, Ce_2O_3, CeO_2 and La_2O_3 were retrieved from FactSage.

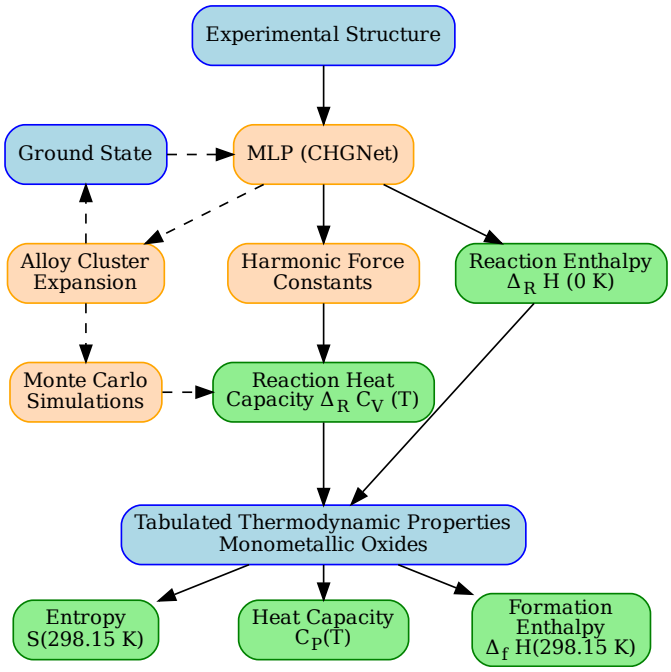

Figure 3.1: Outline of the methodology, with computational steps in blue, thermodynamic calculations in green, and experimental data and ground states in blue.

3.2 Choice of Supercell and Doping Concentrations

Since an orthorhombic structure was used, we were limited to using $Ca_4Mn_4O_{12}$ as the smallest possible unit cell. To explore 5–6 different doping concentrations without introducing excessively high dopant levels, we employed a supercell $2 \times 2 \times 1$, which results in the structure $Ca_{16}Mn_{16}O_{48}$. This choice also accommodates commonly studied doping levels of 25% and 12.5%, allowing a direct comparison with data from the literature. Due to the supercell size, all doping concentrations are in multiples of 1/16, and non-stoichiometric oxygen vacancies are in multiples of 1/48.

Chemical reactions	
Dopant (Site)	Chemical reaction for non-stoichiometric x doping concentration and δ oxygen vacancy
Ti (B)	$\mathrm{CaO} + (1-x-\delta)\,\mathrm{Mn_3O_4} + x\,\mathrm{TiO_2} \Leftrightarrow \mathrm{CaMn_{1-x}Ti_xO_{3-\delta}} + (2-2x-3\delta)\,\mathrm{MnO}$
Fe (B)	$\mathrm{CaO} + (1-x-\delta)\,\mathrm{Mn_3O_4} + x\,\mathrm{Fe_2O_3} \Leftrightarrow \mathrm{CaMn_{1-x}Fe_xO_{3-\delta}} + x\,\mathrm{FeO} + (2-2x-3\delta)\,\mathrm{MnO}$
Cr (B)	$\mathrm{CaO} + (1-x-\delta)\,\mathrm{Mn_3O_4} + x\,\mathrm{CrO_2} \Leftrightarrow \mathrm{CaMn_{1-x}Cr_xO_{3-\delta}} + (2-2x-3\delta)\,\mathrm{MnO}$
Cu (B)	$\mathrm{CaO} + (1-x-\delta)\,\mathrm{Mn_3O_4} + 3x\,\mathrm{CuO} \Leftrightarrow \mathrm{CaMn_{1-x}Cu_xO_{3-\delta}} + x\,\mathrm{Cu_2O} + (2-2x-3\delta)\,\mathrm{MnO}$
Si (B)	$\mathrm{CaO} + (1-x-\delta)\,\mathrm{Mn_3O_4} + x\,\mathrm{SiO_2} \Leftrightarrow \mathrm{CaMn_{1-x}Si_xO_{3-\delta}} + (2-2x-3\delta)\,\mathrm{MnO}$
Mg (B)	$\mathrm{CaO} + (1-x-\delta)\,\mathrm{Mn_3O_4} + x\,\mathrm{MgO} + x\,\mathrm{O_2} \Leftrightarrow \mathrm{CaMn_{1-x}Mg_xO_{3-\delta}} + (2-2x-3\delta)\,\mathrm{MnO}$
Mo (B)	$\mathrm{CaO} + (1-x-\delta)\,\mathrm{Mn_3O_4} + x\,\mathrm{MoO_2} \Leftrightarrow \mathrm{CaMn_{1-x}Mo_xO_{3-\delta}} + (2-2x-3\delta)\,\mathrm{MnO}$
La (A)	$(1-x)\,\mathrm{CaO} + (1-\delta)\,\mathrm{Mn_3O_4} + \frac{x}{2}\,\mathrm{La_2O_3} \Leftrightarrow \mathrm{Ca_{1-x}MnLa_xO_{3-\delta}} + \frac{x}{4}\,\mathrm{O_2} + (2-3\delta)\,\mathrm{MnO}$
Ce (A)	$(1-x)\,\mathrm{CaO} + (1-\delta)\,\mathrm{Mn_3O_4} + x\,\mathrm{Ce_2O_3} \Leftrightarrow \mathrm{Ca_{1-x}MnCe_xO_{3-\delta}} + x\,\mathrm{CeO_2} + (2-3\delta)\,\mathrm{MnO}$
Sr (A)	$(1-x)\,\mathrm{CaO} + (1-\delta)\,\mathrm{Mn_3O_4} + x\,\mathrm{SrO} \Leftrightarrow \mathrm{Ca_{1-x}MnSr_xO_{3-\delta}} + (2-3\delta)\,\mathrm{MnO}$
Bi (A)	$(1-x)\,\mathrm{CaO} + (1-\delta)\,\mathrm{Mn_3O_4} + \frac{x}{2}\,\mathrm{Bi_2O_3} \Leftrightarrow \mathrm{Ca_{1-x}MnBi_xO_{3-\delta}} + \frac{x}{4}\,\mathrm{O_2} + (2-3\delta)\,\mathrm{MnO}$

Table 3.1: Chemical reactions considered for estimating thermodynamical properties of doped $\mathrm{CaMnO_{3-\delta}}$

3.3 Thermodynamic Theory

Following the approach of Brorsson *et al.* [20], the procedure for estimating the thermodynamic properties of a mixed metal oxide is as follows (see Figure 3.1):

1. Identify a suitable chemical reaction that represents the formation of the compound of interest, in this case, doped $\mathrm{CaMnO_3}$, from a set of binary oxides, here Ti-doped $\mathrm{CaMnO_3}$ will be used as an example (all chemical reactions used can be seen in Table 3.1),

$$\mathrm{CaO} + (1-x-\delta)\mathrm{Mn_3O_4} + x\,\mathrm{TiO_2} \Longleftrightarrow \mathrm{CaMn_{1-x}Ti_xO_{3-\delta}} + (2-2x-3\delta)\mathrm{MnO}. \tag{3.1}$$

   where x represents the doping concentration and δ represents the non-stoichiometric oxygen vacancy concentration.
2. Compute the reaction heat capacity at constant volume

$$\begin{aligned}\Delta_{\mathrm{R}}C_V = C_{V,\mathrm{CaMn_{1-x}Ti_xO_{3-\delta}}} - \Big(&C_{V,\mathrm{CaO}} + (1-x-\delta)\,C_{V,\mathrm{Mn_3O_4}} + x\,C_{V,\mathrm{TiO_2}} \\ &- (2-2x-3\delta)C_{V,\mathrm{MnO}}\Big).\end{aligned} \tag{3.2}$$

3. The reaction enthalpy at 0 K was approximated by calculating the change in internal energy, with CHGNet, under the assumption that volume changes are negligible at 0 K,

$$\begin{aligned}\Delta_{\mathrm{R}}H^{0\,\mathrm{K}} &= \Delta_{\mathrm{R}}U^{0\,\mathrm{K}} + P\Delta_{\mathrm{R}}V^{0\,\mathrm{K}} \approx \Delta_{\mathrm{R}}U^{0\,\mathrm{K}} \\ &= U^{0\,\mathrm{K}}_{\mathrm{CaMn_{1-x}Ti_xO_{3-\delta}}} \\ &\quad - \left(U^{0\,\mathrm{K}}_{\mathrm{CaO}} + (1-x-\delta)U^{0\,\mathrm{K}}_{\mathrm{Mn_3O_4}} + xU^{0\,\mathrm{K}}_{\mathrm{TiO_2}} - (2-2x-3\delta)U^{0\,\mathrm{K}}_{\mathrm{MnO}}\right).\end{aligned} \tag{3.3}$$

4. Predict reaction enthalpy and reaction entropy at room temperature 298.15 K.

$$\Delta_{\mathrm{R}} H^{298.15\,\mathrm{K}} \approx \Delta_{\mathrm{R}} H^{0\,\mathrm{K}} + \int_0^{298.15} \Delta_{\mathrm{R}} C_V dT \tag{3.4}$$

$$\Delta_{\mathrm{R}} S^{298.15\,\mathrm{K}} = \Delta_{\mathrm{R}} S^{0\,\mathrm{K}} + \int_0^{298.15} \frac{\Delta_{\mathrm{R}} C_V}{T} dT \tag{3.5}$$

5. Use experimental data of the binary metal oxides from NIST-JANAF to correct formation enthalpy and entropy.

$$\begin{aligned} \Delta_{\mathrm{f}} H^{298.15\,\mathrm{K}}_{\mathrm{CaMn_{1-x}Ti_xO_{3-\delta}}} = {} & \Delta_{\mathrm{R}} H^{298.15\,\mathrm{K}} + \Delta_{\mathrm{f}} H^{298.15\,\mathrm{K}}_{\mathrm{CaO}} \\ & + (1-x-\delta)\Delta_{\mathrm{f}} H^{298.15\,\mathrm{K}}_{\mathrm{Mn_3O_4}} + x\Delta_{\mathrm{f}} H^{298.15\,\mathrm{K}}_{\mathrm{TiO_2}} \\ & - (2-2x-3\delta)\Delta_{\mathrm{f}} H^{298.15\,\mathrm{K}}_{\mathrm{MnO}} \end{aligned} \tag{3.6}$$

$$\begin{aligned} S^{298.15\,\mathrm{K}}_{\mathrm{CaMn_{1-x}Ti_xO_{3-\delta}}} = {} & \Delta_{\mathrm{R}} S^{298.15\,\mathrm{K}} + S^{298.15\,\mathrm{K}}_{\mathrm{CaO}} \\ & + (1-x) S^{298.15\,\mathrm{K}}_{\mathrm{Mn_3O_4}} + x S^{298.15\,\mathrm{K}}_{\mathrm{TiO_2}} \\ & - 2(1-x) S^{298.15\,\mathrm{K}}_{\mathrm{MnO}} \end{aligned} \tag{3.7}$$

6. Calculating the heat capacity. In Brorsson *et al.* [20] they demonstrated how the heat capacity can be extended to elevated temperatures. The extension relies on the assumption that two expressions for the enthalpy of formation are equivalent:

$$\Delta_f H^T = \Delta_f H^{0K} + \int_0^T C_p \, dT' \tag{3.8}$$

and

$$\begin{aligned} \Delta_f H^T_{\mathrm{CaMn_{1-x}Ti_xO_{3-\delta}}} \approx {} & \Delta_R H^{0K} + \int_0^T \Delta_R C_V \, dT' + \Delta_f H^T_{\mathrm{CaO}} + x\,\Delta_f H^T_{\mathrm{TiO_2}} \\ & + (1-x-\delta)\,\Delta_f H^T_{\mathrm{Mn_3O_4}} - (2-2x-3\delta)\,\Delta_f H^T_{\mathrm{MnO}}. \end{aligned} \tag{3.9}$$

Equating these two leads to an approximate expression for the integrated heat capacity:

$$\begin{aligned} \int_0^T C_p \, dT' \approx {} & -\Delta_f H^{0K} + \Delta_R H^{0K} + \int_0^T \Delta_R C_V \, dT' \\ & + \Delta_f H^T_{\mathrm{CaO}} + x\Delta_f H^T_{\mathrm{TiO_2}} + (1-x-\delta)\Delta_f H^T_{\mathrm{Mn_3O_4}} \\ & - (2-2x-3\delta)\Delta_f H^T_{\mathrm{MnO}}. \end{aligned} \tag{3.10}$$

Following the approach of Gastaldi *et al.* [12] for calculating thermodynamic properties of $CaMnO_3$ with oxygen vacancies, tabulated reference data for the binary oxides are used to improve accuracy. The thermochemical data for CaO are taken from the NIST-JANAF tables, while values for Mn_3O_4 and MnO are

obtained from other studies [26, 27]. Each formation enthalpy term is defined by

$$\Delta_f H_X^T = \Delta_f H_X^0 + \int_0^T C_{p,X}\, dT', \tag{3.11}$$

where $X \in \{\mathrm{CaO}, \mathrm{Mn_3O_4}, \mathrm{MnO}, \mathrm{TiO_2}\}$. Substituting these expressions into the previous equation allows the compound's heat capacity to simplified to

$$\begin{aligned} C_P(T) \approx{}& \Delta_R C_V(T) + C_{P,\mathrm{CaO}}(T) \\ &+ (1 - x - \delta) C_{P,\mathrm{Mn_3O_4}}(T) + x C_{P,\mathrm{TiO_2}}(T) \\ &- (2 - 2x - 3\delta) C_{P,\mathrm{MnO}}(T). \end{aligned} \tag{3.12}$$

3.4 Finding the Ground State

To generate training structures for cluster expansion, `ICET`'s structure annealing method was used to sample 400 configurations, with the weighting biased towards higher entropy configurations. This approach allocates more training structures to higher doping concentrations, reflecting their larger configurational space. The sampled structures were then relaxed using CHGNet, and the resulting data set was used to build an `ICET` structure container for cluster expansion training.
The final structure container used pair interaction cutoffs of approximately 7.0 Å and triplet cutoffs of about 5.4 Å. For certain dopants, these cutoffs had to be reduced slightly due to a high condition number.
For modeling oxygen vacancies in doped $CaMnO_3$, the previously identified ground-state structures were used as primitive cells to generate 300 training configurations. Because of the significant reduction in symmetry when vacancies are introduced, often lowering the crystal class from orthorhombic to triclinic, shorter cutoff distances were required. Typical cutoff ranges were 4.5–3.5, Å for pair interactions and 2.5–1.5, Å for triplets.
In the case of Si doping, introducing oxygen vacancies resulted in an incompatible sublattice, and attempts to work around this led to an unacceptably high condition number. For Fe doping at a concentration of 2/16, the complete loss of symmetry made it difficult to generate a valid structure container without reducing the cutoffs to inaccurately low values. As a result, they were excluded from further analysis.
Once the structure containers were assembled, cluster expansions were trained using an automatic relevance determination regression (ARDR) method. A line scan was performed to optimize the regularization threshold λ. The ground states were then determined using `ICET`'s `GroundStateFinder`, which applies mixed-integer programming to identify the minimum-energy configuration.

3.5 Training Force Constant Potential

To compute the phononic heat capacity, the force constants must first be determined, as they describe the response of atoms to small displacements. These force

constants are then used to calculate the phonon frequencies from which the vibrational contribution to the heat capacity is obtained, as detailed in the Theory section.
In this work, the force constants were extracted using the `hiPhive` Python package. For doped compounds without oxygen vacancies, 150 supercell structures (each with 280 atoms) were used, while 50 structures sufficed for systems with vacancies, balancing computational efficiency and accuracy. The low symmetry of the systems leads to a large number of degrees of freedom and orbit parameters, ranging from 1,000 to 10,000. To ensure that the system is well overdetermined, a substantial dataset of force constants was generated: approximately 150,000 from 150 structures and 50,000 from 50 structures. The cutoff distances were set to $0.4a$ and $0.2a$, with a being the smallest lattice parameter. Given the large size of the dataset, cross-validation was less necessary and ARDR was too computationally costly. Instead, ridge regression with a low regularization parameter ($\alpha = 0.01$) was used.

3.6 Monte Carlo Simulations

Monte Carlo simulations were performed using the `ICET` library and its `mchammer` sub-module to study the thermodynamic behavior of doped $CaMnO_3$ systems, both with and without oxygen vacancies. Simulations were carried out in the canonical ensemble (N_iVT), using supercells of 480 atoms (including potential vacancies) and 8 000 Monte Carlo cycles for adequate sampling.

3.7 FactSage Phase Diagram Construction

Phase diagrams were constructed using FactSage [25] by first manually compiling a comprehensive FactSage database of all compounds, including various doping concentrations and oxygen vacancy levels, along with their formation enthalpy, entropy at 298.15 K, and heat capacity parameters fitted to the function $k_1 + k_2T^{-2} + k_3T^{-0.5} + k_4T^{-3}$. For each doped material, a reaction was defined that involved the doped compound and oxygen gas (O_2). The Gibbs free energy of all possible phases was then calculated by FactSage as a function of temperature and oxygen partial pressure. Phase stability was determined by identifying the phase or mix of phases with the minimum Gibbs free energy under the given conditions, including all compounds from FactPS and FToxid FactSage databases [25].

3.8 Periodic Table Screening via Bartel Tolerance Factor

To assess the perovskite stability of doped $CaMnO_3$, we evaluated the systems using the Bartel tolerance factor [28], with a threshold value of $\tau = 4.18$, below which structures are generally considered stable and above which they are likely unstable. For each dopant element, its suitability for substitution at the A-site or B-site was assessed based on the following criteria:

- **Oxidation state:** The oxidation state with the smallest net charge difference.
- **Coordination number:** Ionic radii were used with 12-fold coordination for the A-site and 6-fold for the B-site.
- **Spin:** For some valence states, e.g. Cr^{+2}, there were values for high and low spin, for these the lower and better tolerance factor was considered. As a result, e.g. Cr at the A-site goes from above the threshold 4.196 (high spin) to 4.178 (low spin).

The Bartel tolerance factor was computed as follows:

$$\tau = \frac{r_X}{r_B} - n_A \left(n_A - \frac{r_A/r_B}{\ln\left(r_A/r_B\right)} \right) \tag{3.13}$$

where r_A and r_B are the ionic radii of the A-site and B-site cations, and $r_X = r_O = 1.40$ Å is the ionic radius of oxygen. When doping is used, the average ionic radii at the A- and B-sites are taken instead, as well as the average oxidation state of A. The data for ionic radii were taken from the Shannon Database of ionic radii [29]. The results from the Bartel tolerance factor screening were intended to serve as an additional metric for assessing stability, complementing the thermodynamic data and phase diagram analysis. In addition, they provide a useful guide for future work. Since this screening was conceived and carried out towards the end of the project, it did not influence the initial selection of dopants considered in this study.

4

Results & Discussion

The primary objective of this work is to conduct a comprehensive screening of the thermodynamic properties and phase stability of a wide range of doped $CaMnO_3$ compositions. By casting a broad net over various dopants and doping concentrations, this study aims to explore the potential for discovering new materials with enhanced performance as oxygen carriers in chemical looping combustion. It is important to acknowledge that some of the investigated compositions may pose challenges in terms of experimental synthesis and practical implementation, which remains an open question since there is currently limited information available in the literature regarding these doped systems.

4.1 Configurational Heat Capacity & Reaction Heat Capacity

In this section, a representative example is presented to highlight order–disorder transitions. It serves to visualize the configurational and reaction heat capacities, which are central to the calculation of thermodynamic properties. Figure 4.1 displays these heat capacities for Ti-doped $CaMnO_3$.

In the top sub-figure, prominent peaks in the heat capacity are observed, with a clear shift toward lower temperatures and broadening as the Ti doping concentration decreases. This behavior is indicative of an order–disorder phase transition [30], where the system evolves from a low-probability Mn–Ti site switching to a more disordered state. The configurational heat capacities of the other dopants can be seen in Appendix A.

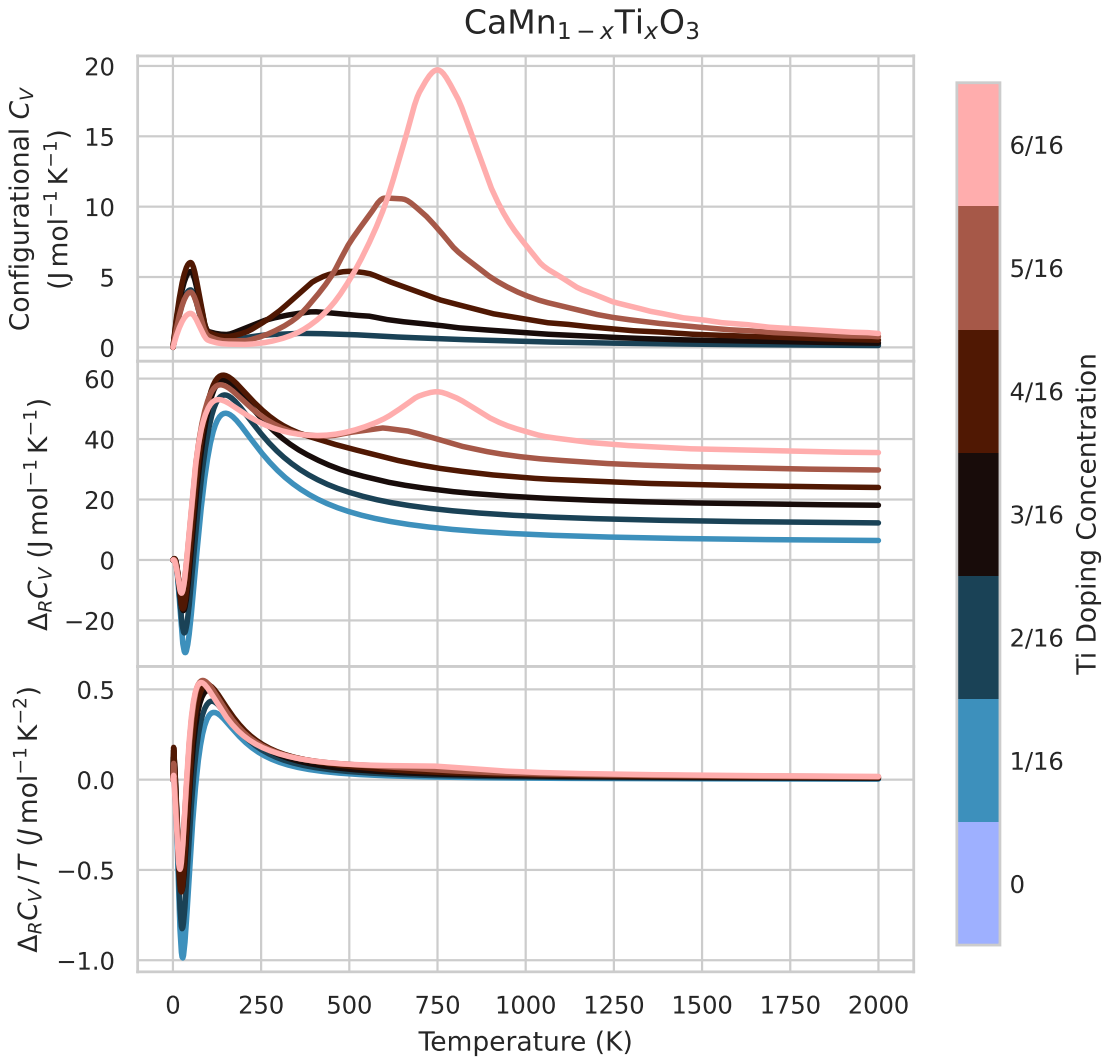

Figure 4.1: Reaction heat capacity $\Delta_R C_V$, $\Delta_R C_V/T$, and configurational heat capacity C_V for Ti-doped $CaMnO_3$ as a function of temperature.

Figure 4.2 presents the corresponding heat capacities for Ti-doped $CaMnO_3$ containing oxygen vacancies. In this case, the peaks are broader and exhibit more noise, with the variance decaying more gradually and increasing with higher vacancy concentrations. Additionally, when examining $\Delta_R C_V$, no clear gradual trends are observed, unlike the smoother, more systematic behavior seen in vacancy-free Ti-doped $CaMnO_3$. This noisier configurational C_V in compounds with oxygen vacancies may result from a less accurate cluster expansion fit, leading to a poorer estimation of the ground state. This discrepancy in the cluster expansion for systems with oxygen vacancies is discussed at the end of this chapter.

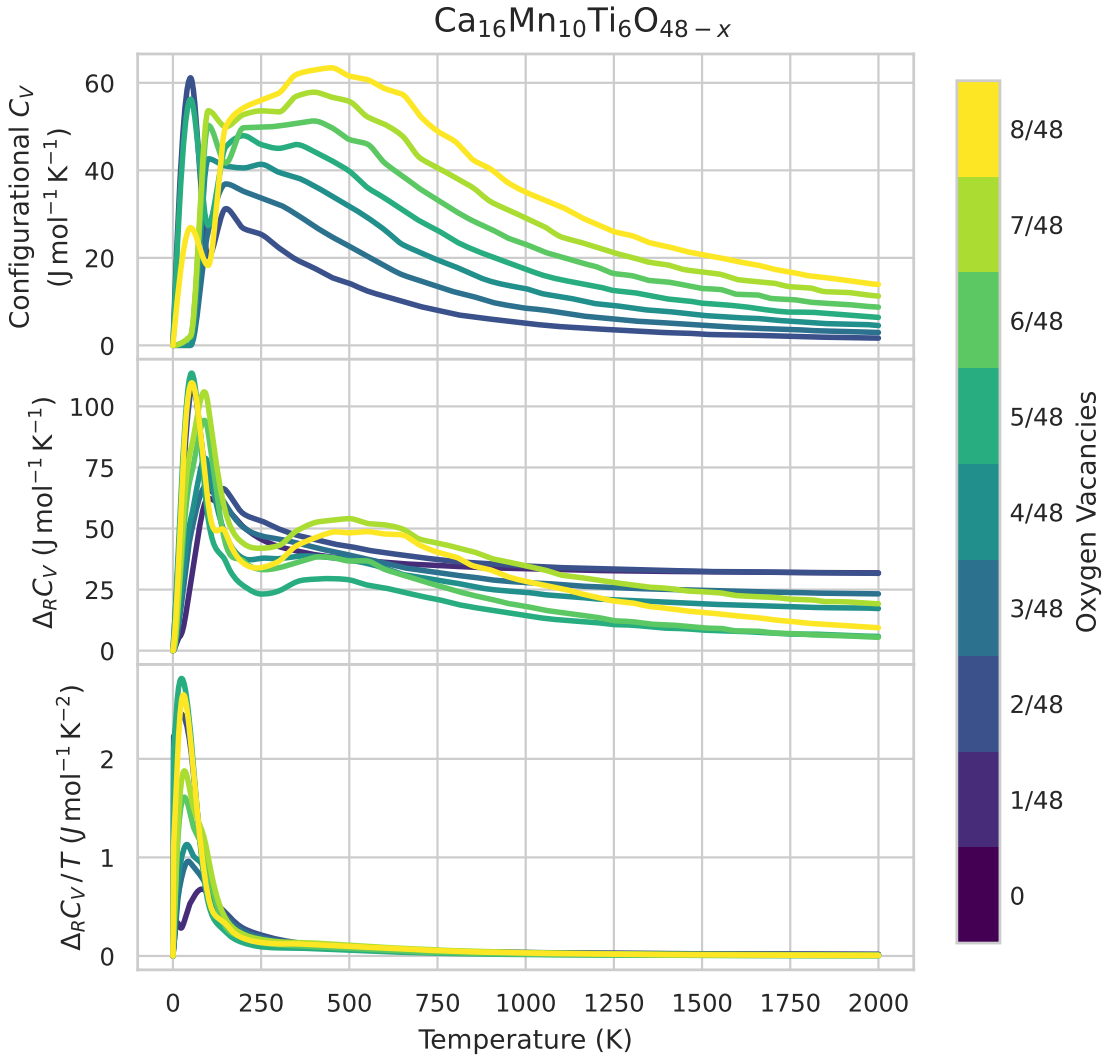

Figure 4.2: Reaction heat capacity $\Delta_R C_V$, $\Delta_R C_V/T$, and configurational heat capacity C_V for Ti-doped $CaMnO_3$ with varying amount of oxygen vacancies, $1/48, 2/48, ..., 8/48$.

In particular, the reaction heat capacity $\Delta_R C_V$ becomes negative around 25–30 K for Ti-doping (Figure 4.1). This behavior arises from the larger number of low-frequency phonon modes (0–2.5 THz) in Mn_3O_4 compared to $CaMnO_3$; see Figure 4.3. The phonon density of states (DOS) represents the number of vibrational modes (phonons) available at each frequency, which directly influences thermal properties, such as heat capacity. A negative $\Delta_R C_V$ is not problematic in itself, as it refers to the heat capacity of the reaction, not that of an individual material.

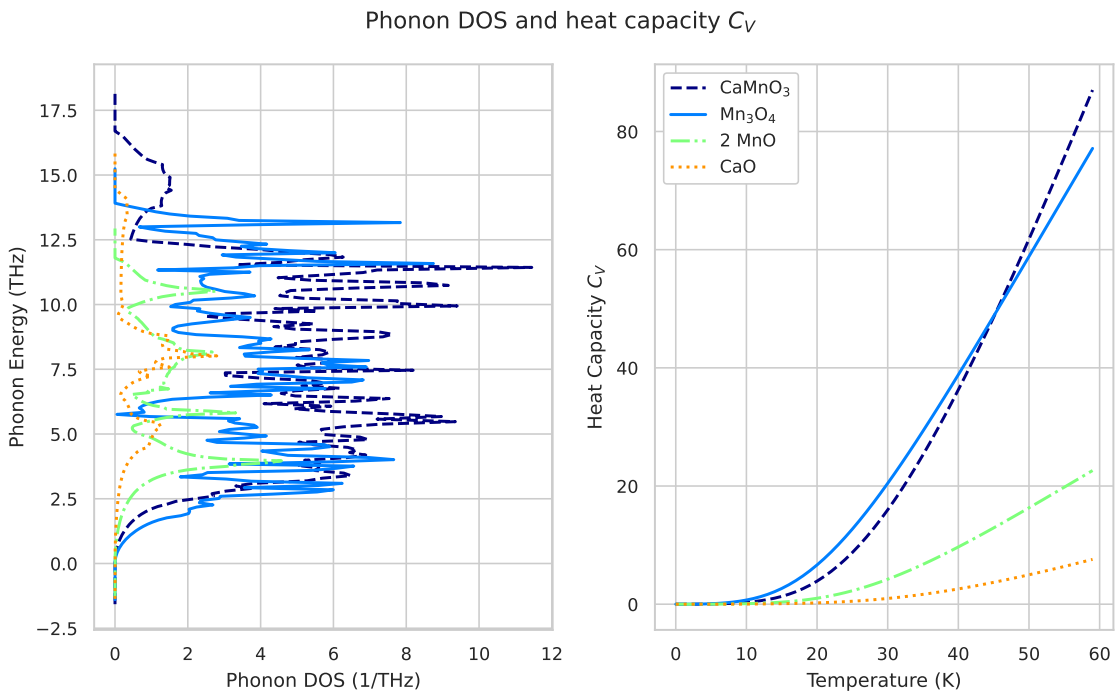

Figure 4.3: Phonon density of states and phononic heat capacity C_V for the reaction with pristine $CaMnO_3$ ($CaO + Mn_3O_4 \Longleftrightarrow CaMnO_3 + 2MnO$).

While the configurational heat capacity provides valuable insight into the degree of disorder, the primary focus lies in the formation enthalpy, as it serves as a direct indicator of thermodynamic stability.

4.2 Thermodynamic Properties

In general, the availability of reference data to validate thermodynamic properties is limited, particularly for doped or oxygen-deficient $CaMnO_3$ systems. However, for pristine $CaMnO_3$, experimental data are available and serve as a reliable reference. As shown in Figure 4.4, the calculated heat capacity shows only minor deviations from the values reported in FactSage and by Bakken *et al.* [31]. The formation enthalpy shows a noticeable discrepancy compared to experimental results, but still falls within the typical uncertainty margin of $\pm 10\%$, as noted by Gastaldi *et al.* [12].

A smaller discrepancy is observed in the entropy values: this work yields $S = 84.73\,\mathrm{J\,/\,(mol\,K)}$ at $298.15\,\mathrm{K}$, which is lower than the $96.32\,\mathrm{J\,/\,(mol\,K)}$ reported by Gastaldi *et al.* [12]. This difference is particularly interesting given the use of a largely equivalent methodology. It may be attributed to the use of CHGNet in this work instead of DFT calculations based on VASP. In contrast, the formation enthalpy shows very close agreement, with the calculated value of $\Delta H_f = -1.192 \times 10^6\,\mathrm{J/mol}$ (at $298.15\,\mathrm{K}$) compared to the computational value of $\Delta H_f = -1.189 \times 10^6\,\mathrm{J/mol}$ reported by Gastaldi *et al.* [12].

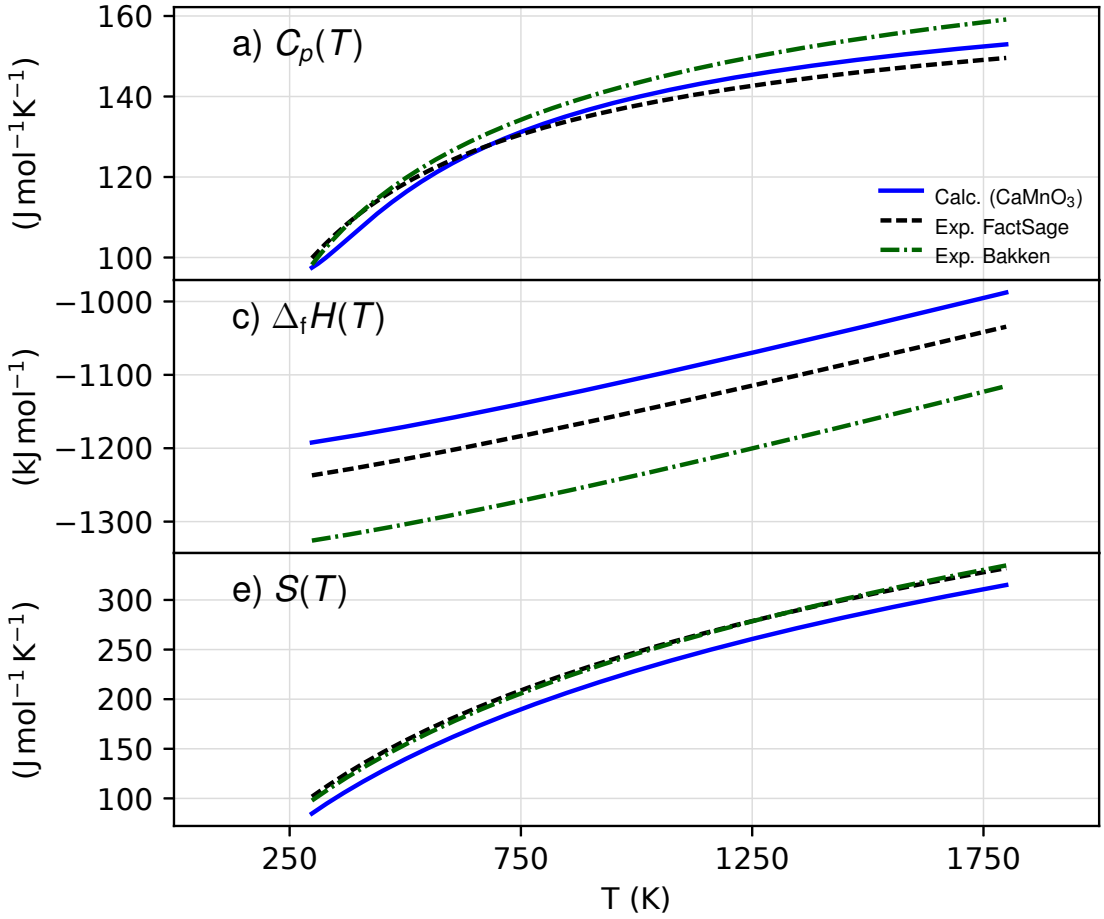

Figure 4.4: Comparison of formation enthalpy $\Delta_f H$, entropy S and heat capacity C_P for $CaMnO_3$ as a function of temperature, from this work, FactSage, and Bakken [31].

For doped systems, there are limited experimental data available for validation. However, computational data from the FactSage database (AIMP) can be used for comparison. As shown in Figure 4.5, the formation enthalpy values obtained in this work show good agreement with those reported in the FactSage database, supporting the consistency of the computational approach.

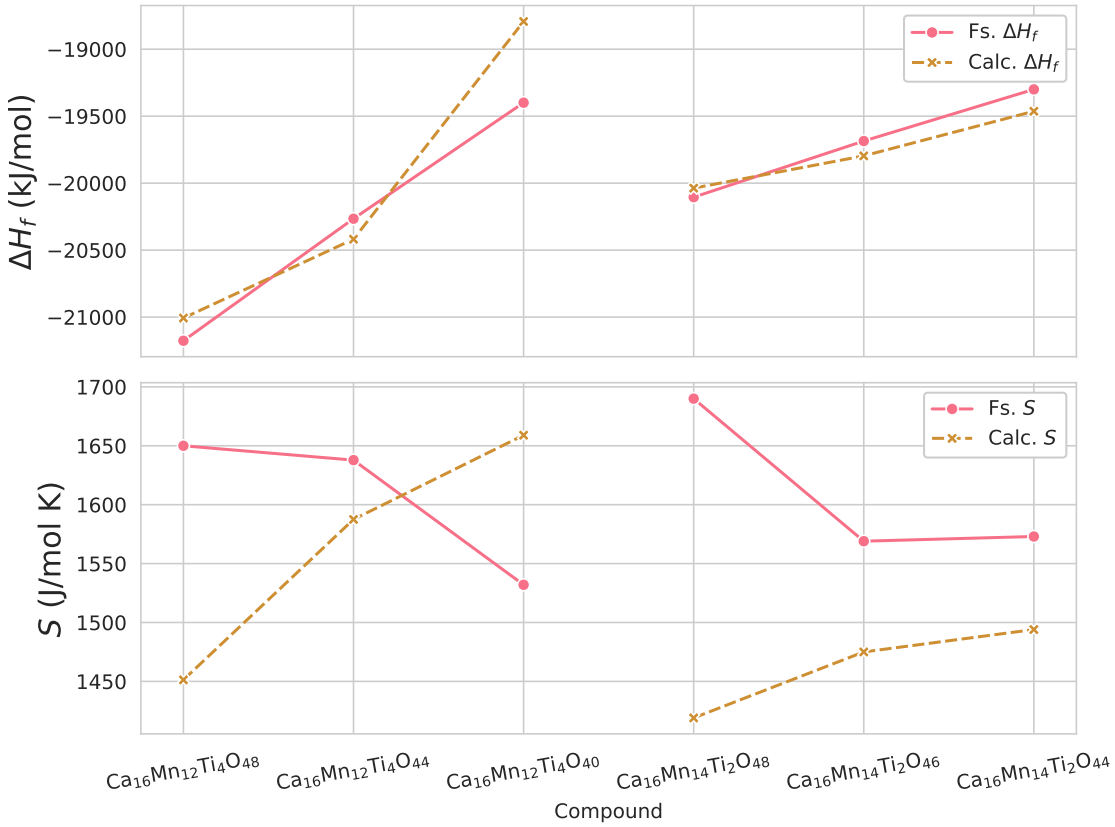

Figure 4.5: Comparisons of the formation enthalpy ($\Delta_f H$) and entropy (S) at 298.15 K for Ti-doped $CaMnO_{3-\delta}$ with computational data from FactSage. "Fs." denotes FactSage data points, while "Calc." refers to values obtained in this work.

When examining the thermodynamic properties of doped $CaMnO_3$, Figure 4.6 illustrates the case of Ti-doping again as a representative example. Doping generally has a significant impact on the formation enthalpy, though some exceptions will be discussed later. Notably, the change in formation enthalpy due to doping appears largely temperature independent. This indicates that evaluating the formation enthalpy at a single temperature, such as 298.15 K, is sufficient for assessing trends. Additionally, the relatively minor changes in entropy upon doping imply that the formation enthalpy is the dominant contribution to the Gibbs free energy, making it a reliable metric for evaluating thermodynamic stability.

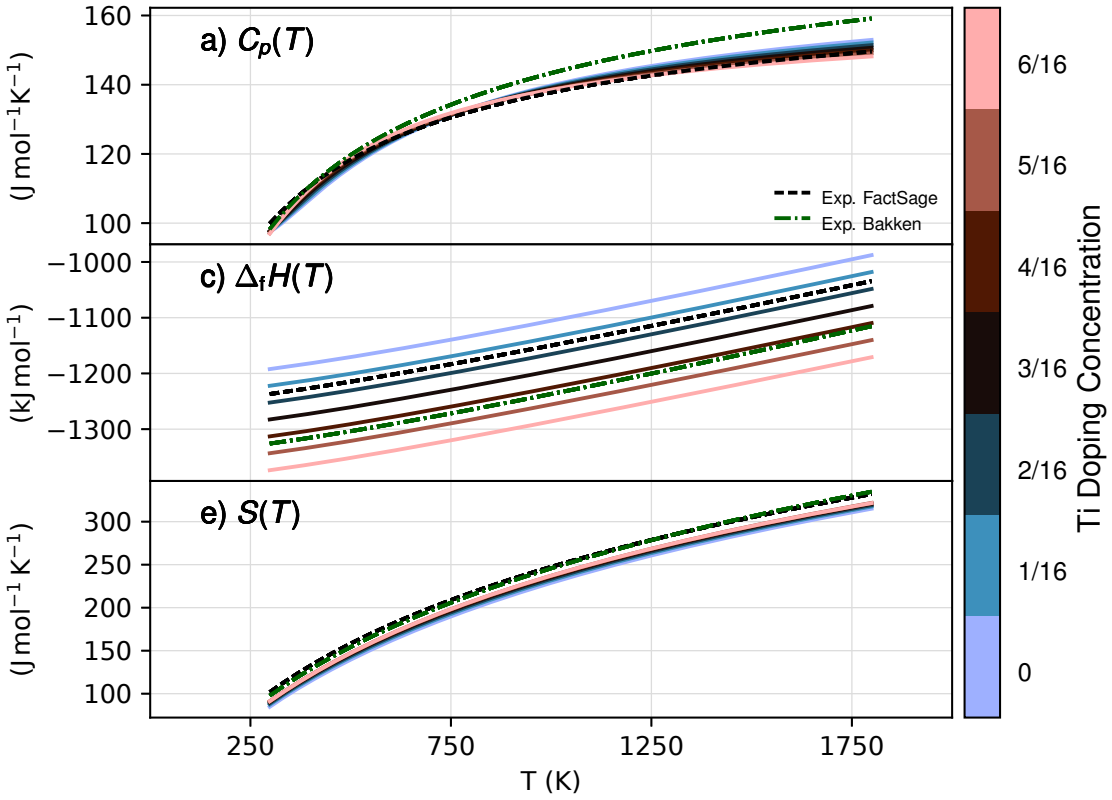

Figure 4.6: Thermodynamic properties of Ti-doped $CaMnO_3$: Heat capacity C_p, formation enthalpy ΔH_f, and entropy S.

4.3 Formation Enthalpy for Doped $CaMnO_3$

As shown in Figure 4.7, the formation enthalpy ΔH_f at 298.15 K for $CaMnO_3$ with different dopants at the A- and B-sites in relation to pristine $CaMnO_3$ varies significantly. Dopants such as Ce, Ti, La, Si, and Mo lower the formation enthalpy, indicating a stabilizing effect on the system. In contrast, Bi, Cr, and Cu increase the formation enthalpy, suggesting they destabilize the system. Sr, Fe, and Mg have little effect on the formation enthalpy. Additionally, Si is unlikely to be stable on B-site due to its high Bartel tolerance factor (see Section 4.6).

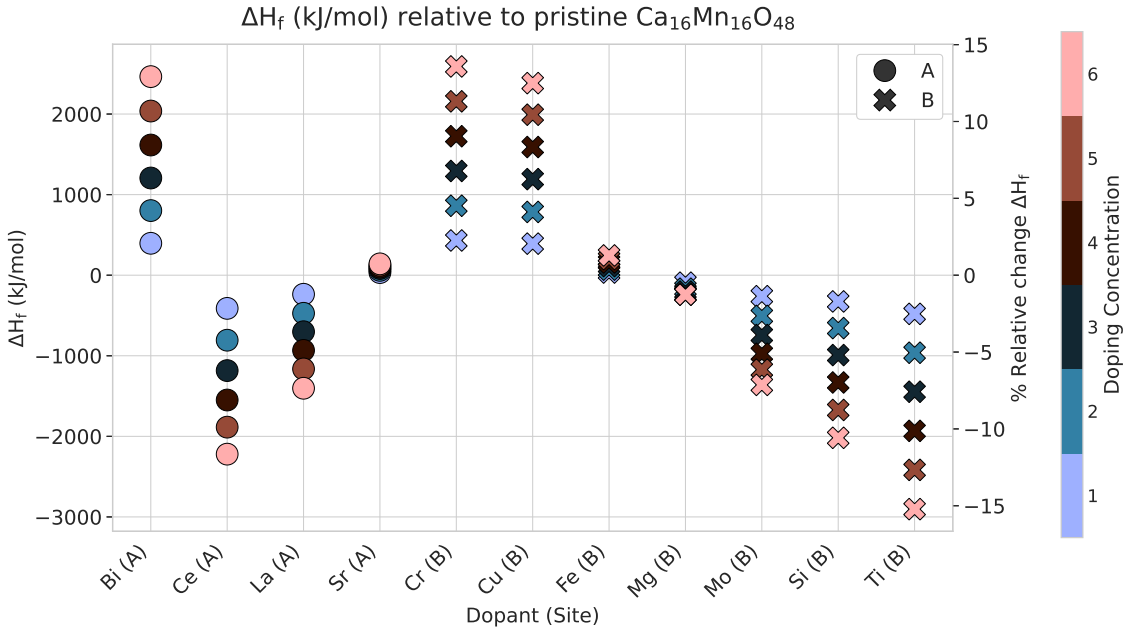

Figure 4.7: Formation enthalpy (ΔH_f) at 298.15 K for $CaMnO_3$ doped with various elements at both A- and B-sites at concentrations of 1/16, 2/16, ..., 6/16. Note that the values correspond to the entire supercell that is 16 times larger than pristine $CaMnO_3$.

4.4 Formation Enthalpy for Doped $CaMnO_{3-\delta}$ With Oxygen Vacancies

To assess the thermodynamic stability of doped $CaMnO_3$ with oxygen vacancies, the formation enthalpy ΔH_f at 298.15 K is compared across different dopants and vacancy concentrations. The results, summarized in Figure 4.8 and Figure 4.9, show the variation in ΔH_f in relation to pristine $CaMnO_3$ as a function of dopant type, site, and concentration (2/16, 4/16, and 6/16 dopant substitution levels), as well as for structures with oxygen vacancies ranging from 1/48 to 8/48. For context, a vacancy concentration of 8/48 corresponds to an oxygen loss of approximately 5.59 wt%, as a reference for estimating the extent of material reduction.

The effect of oxygen vacancies is also evident. As vacancy concentration increases (from 1/48 to 8/48), the formation enthalpy generally rises, reflecting the cost associated with introducing oxygen deficiencies. This trend is consistent with expectations, as oxygen vacancies disrupt metal–oxygen bonds.

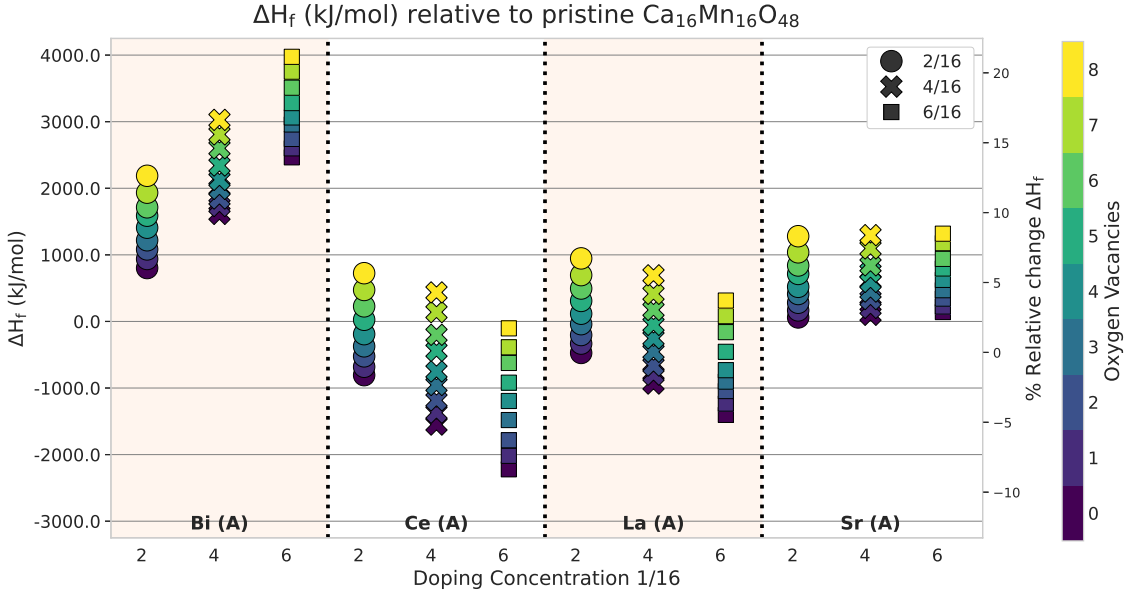

Figure 4.8: Formation enthalpy (ΔH_f) at 298.15 K for $CaMnO_3$ doped with various elements at the A-site at concentrations of 2/16, 4/16, and 6/16, as well as for oxygen vacancies ranging from 1/48 to 8/48. Note that the values correspond to the entire supercell that is 16 times larger than pristine $CaMnO_3$

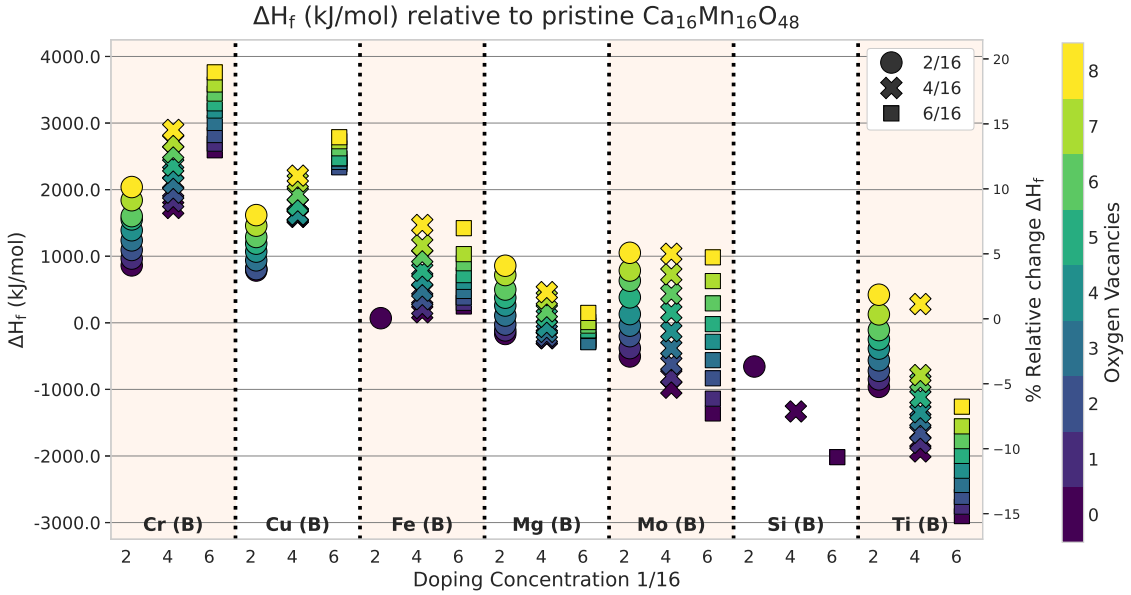

Figure 4.9: Formation enthalpy (ΔH_f) at 298.15 K for $CaMnO_3$ doped with various elements at the B-site at concentrations of 2/16, 4/16, and 6/16, as well as for oxygen vacancies ranging from 1/48 to 8/48. Note that the values correspond to the entire supercell that is 16 times larger than pristine $CaMnO_3$

Figures 4.10,4.11 show the change in formation enthalpy upon creation of an oxygen vacancy for $CaMnO_3$ substitutionally doped at A- and B-site, and concentrations (2/16, 4/16, 6/16). For example, with 6/16 Ti-doping

$$\Delta H_f(\mathrm{Ca_{16}Mn_{10}Ti_6O_{47-x}}) - \Delta H_f(\mathrm{Ca_{16}Mn_{10}Ti_6O_{48-x}}),\ x = 0, ..., 7. \tag{4.1}$$

Among the dopants, Fe, Ti, Sr, and Ce form thermodynamically stable compounds according to the phase diagram analysis presented in the next section. Notably, Sr and Fe exhibit a significantly smaller increase in formation enthalpy upon oxygen vacancy formation compared to Ti and Ce. This suggests that Sr- and Fe-doped $CaMnO_3$ can more easily accommodate oxygen vacancies. This trend is consistent with their behavior in the phase diagrams. Most dopants stay in the range 1-3 eV per oxygen vacancy (see second y-axis), with Cu and Mg going down to 0.5 eV.

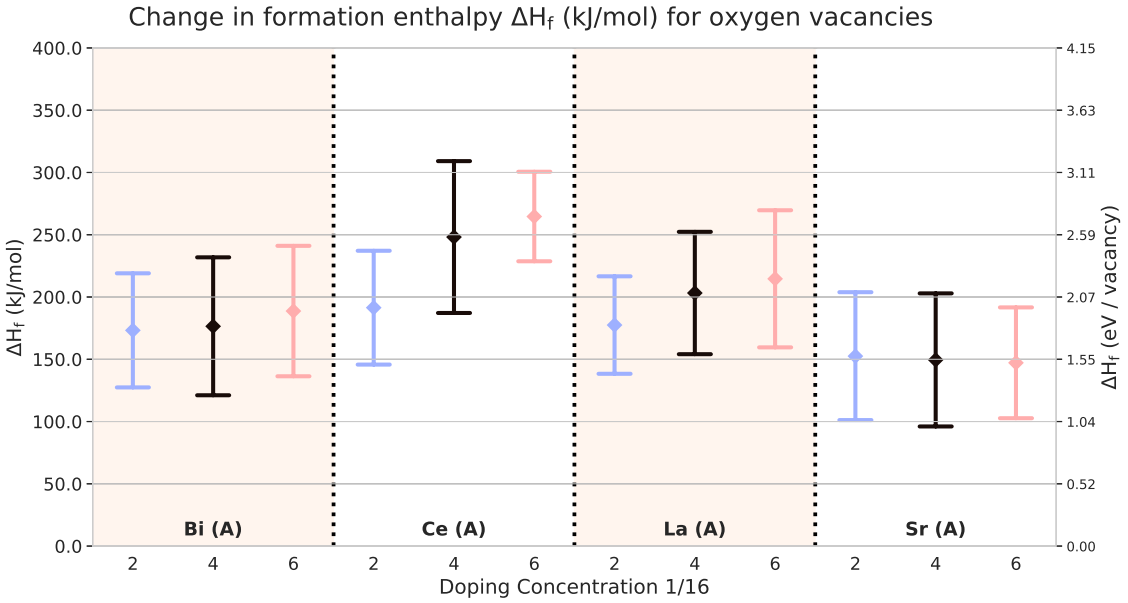

Figure 4.10: Change in formation enthalpy (ΔH_f) for forming an oxygen vacancies at 298.15 K for $CaMnO_3$ doped with various elements at the A-site at concentrations of 2/16, 4/16, and 6/16. The error bars show the ± standard deviation. Note that the values correspond to the entire supercell that is 16 times larger than pristine $CaMnO_3$. The second y-axis shows the change energy in eV per oxygen vacancy.

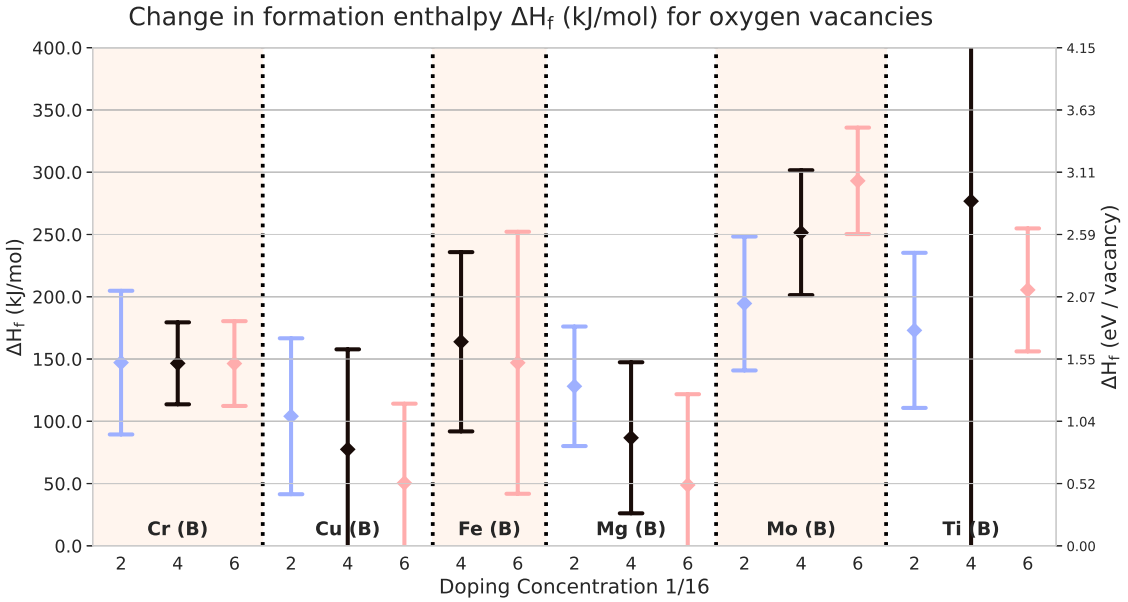

Figure 4.11: Change in formation enthalpy (ΔH_f) for forming an oxygen vacancy at 298.15 K for $CaMnO_3$ doped with various elements at the B-site at concentrations of 2/16, 4/16, and 6/16. The error bars show the ± standard deviation. Note that the values correspond to the entire supercell that is 16 times larger than pristine $CaMnO_3$. The second y-axis shows the change energy in eV per oxygen vacancy.

4.5 Phase Stability of Doped $CaMnO_{3-\delta}$

Equilibrium phase diagrams for doped $CaMnO_{3-\delta}$ were computed using FactSage to assess the thermodynamic stability of oxygen-deficient perovskites under varying oxygen partial pressure (p_{O_2}) conditions. Factsage calculates the thermodynamic equilibrium of multi component and multi phase systems, using a variety of extensive databases (FactPS, FToxid) [25]. Across a range of dopants (Fe, Ti, Ce, and Sr), the perovskite phase remains stable at low temperatures and relatively high oxygen partial pressures, reflecting the oxidized stoichiometry typical of ambient or slightly oxidizing conditions. As the temperature increases and $\log_{10}(p(O_2)/\text{atm})$ decreases, the formation of oxygen vacancies is thermodynamically favored, stabilizing oxygen-deficient phases. This behavior supports the use of these materials in high-temperature environments (typically 800-1000 °C) and across a wide range of oxygen partial pressures, as seen in chemical looping combustion [5].
It should be noted that the formation enthalpies for pure CaMnO3 calculated in this work and in previous studies by Gastaldi *et al.*, differs somewhat from that reported in the literature [31, 25]. It is not fully established what the reason for this deviation is, but it should be acknowledged that there is rather limited experimental data available, in addition to difficulties in retrieving correct data for non-stoichiometric material. To ensure consistency between our calculated formation enthalpies and the experimental values reported in the FactSage database (FToxid), a correction was applied based on the difference between our computed $CaMnO_3$ reference and the experimental formation enthalpy. This correction amounted to −45 kJ/mol

for non-stoichiometric doped $CaMnO_3$, and was 16 times larger for stoichiometric $Ca_{16}Mn_{16}O_{48}$ systems, reflecting the greater formula size.

This correction is necessary because the focus is on comparing doped $CaMnO_3$ phases with experimentally reported compounds in FactSage. Therefore, it is essential to establish a baseline that is consistent with experimental data.

Dopants Cr, Cu, Bi, and Mg were found to be completely unstable all regions of temperature and oxygen partial pressure. As a result, the phase diagrams for these dopants were not included in this analysis. Additionally, Si was excluded due to computational issues related to structures with oxygen vacancies, as discussed earlier. Dopants La (section 4.5.5) and Mo (section 4.5.2) were partly stable where the fully oxidized phases were present but the reduced perovskite phases were rarely stable.

All thermodynamic values used, after correction, for the phase diagram are available in Appendix B.

4.5.1 Fe-doped $CaMnO_{3-\delta}$

The phase stability of Fe-doped $CaMnO_{3-\delta}$ (Figure 4.12) shows that the fully oxidized phase is stable for $\lesssim 500\,\mathrm{K}$ and high $\log_{10} p(O_2)/\mathrm{atm}$. When increasing the temperature, it quickly reduces to $Ca_{16}Mn_{10}Fe_6O_{47}$ as early as $\sim 500\,\mathrm{K}$ and $\log_{10} p(O_2)/\mathrm{atm} \approx -1$. At around $1000\,\mathrm{K}$ and $\log_{10} p(O_2)/\mathrm{atm} \approx -5$, it fully reduces to $Ca_{16}Mn_{10}Fe_6O_{40}$. This stepwise and reversible reduction over a broad temperature and oxygen partial pressure range is a positive indicator of good oxygen carrier properties, as it suggests efficient oxygen release and uptake under relevant operating conditions.

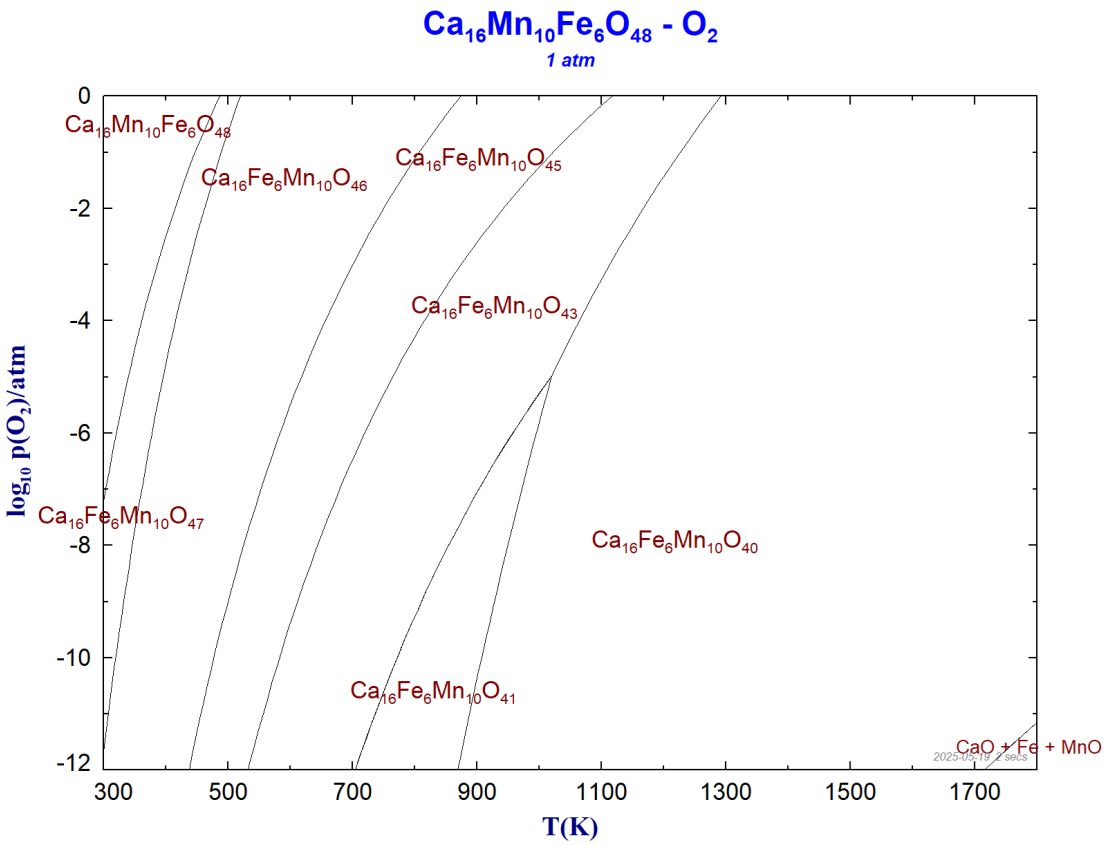

Figure 4.12: Phase stability diagram of Fe-doped $CaMnO_{3-\delta}$ as a function of temperature and oxygen partial pressure ($\log_{10} p(O_2)/\text{atm}$), calculated using FactSage.

4.5.2 Mo-doped $CaMnO_{3-\delta}$

Mo-doped $CaMnO_{3-\delta}$ is generally unstable, as shown in the phase diagram (Figure 4.13), with no reduced perovskite phases present. This absence of accessible oxygen-deficient phases suggests limited redox activity, making Mo a poor candidate for oxygen carrier applications. However, as will be discussed later for La-doping, this apparent instability of the reduced phase may result from challenges in training the CE model for oxygen vacancies. This issue was not present for the fully oxidized phases, which is present in this phase diagram.

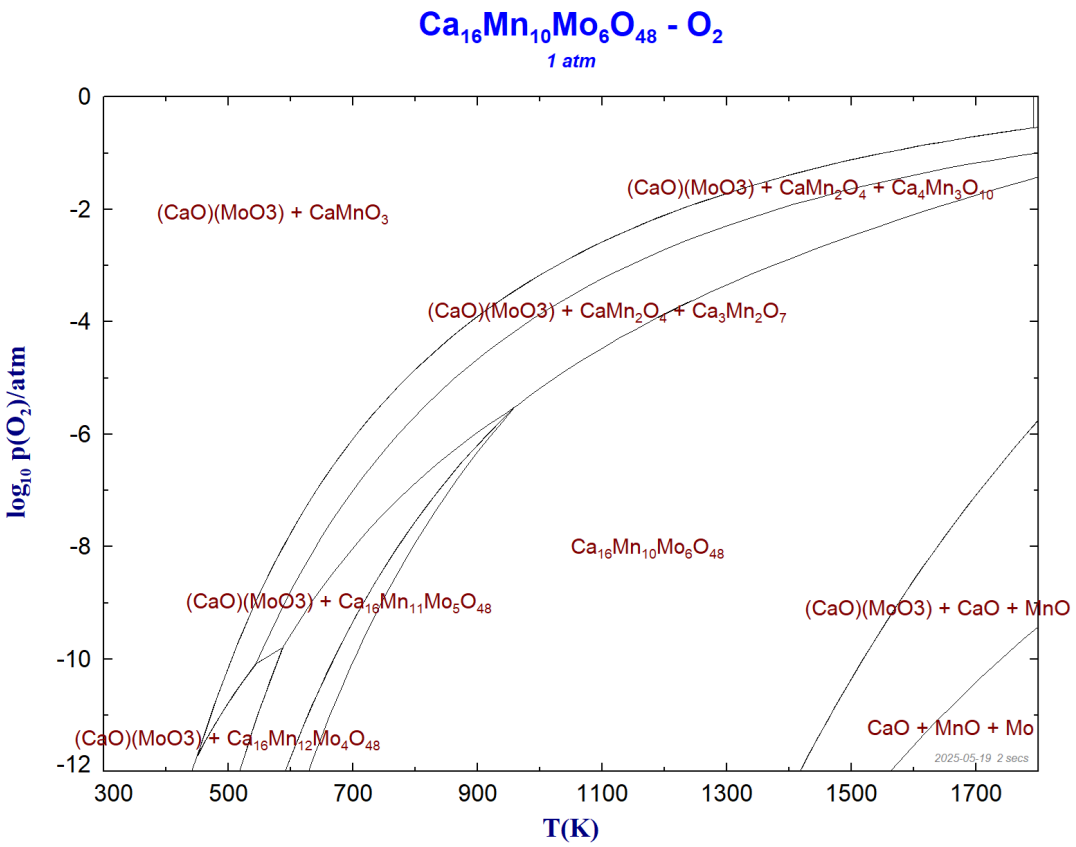

Figure 4.13: Phase stability diagram of Mo-doped $CaMnO_{3-\delta}$ as a function of temperature and oxygen partial pressure ($\log_{10} p(O_2)/\text{atm}$), calculated using FactSage.

4.5.3 Ti-doped $CaMnO_{3-\delta}$

The phase stability of Ti-doped $CaMnO_{3-\delta}$ (Figure 4.14) indicates that the fully oxidized phase remains stable up to approximately 700 K. In contrast to Fe doping, the formation of a reduced phase is significantly more challenging, highlighting greater structural stability but requiring higher temperatures and lower $\log_{10}(p(O_2)/\text{atm})$ to induce oxygen vacancy formation. This suggests that while Ti-doped $CaMnO_{3-\delta}$ may exhibit lower reactivity under moderate conditions, it could offer improved cyclic durability and resistance to phase decomposition (here decomposition refers to the complete breakdown into other oxides) which are advantageous traits for long-term oxygen carrier performance. Of the different dopants considered in this study, Ti appears to be among the most promising. This aligns with previous experimental findings, where Ti-doped $CaMnO_3$ has demonstrated promising performance as an oxygen carrier, including high reactivity and enhanced stability under chemical looping combustion conditions [32].

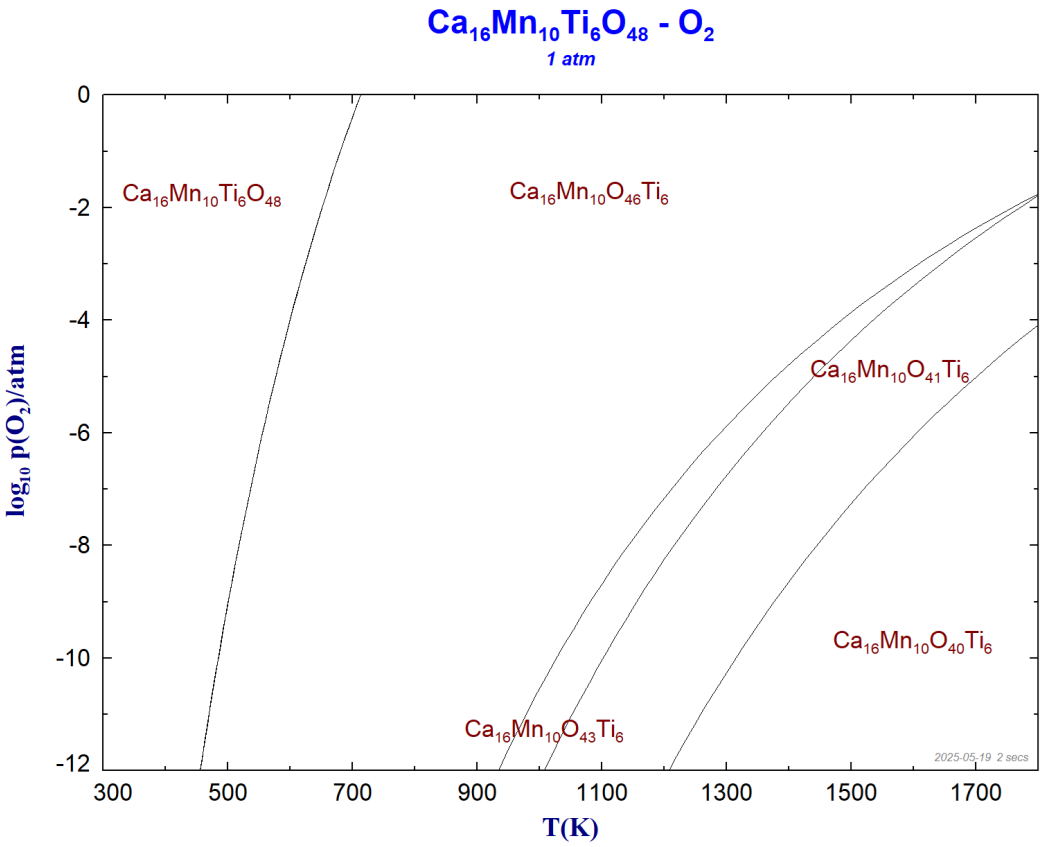

Figure 4.14: Phase stability diagram of Ti-doped $CaMnO_{3-\delta}$ as a function of temperature and oxygen partial pressure ($\log_{10} p(O_2)/\text{atm}$), calculated using FactSage.

4.5.4 Ce-doped $CaMnO_{3-\delta}$

The phase stability of Ce-doped $CaMnO_{3-\delta}$ (Figure 4.15) demonstrates that the fully oxidized phase remains stable over an even broader range of conditions compared to Ti doping. It persists to higher temperatures and lower oxygen partial pressures, indicating enhanced resistance to reduction. This increased stability suggests that oxygen vacancy formation in Ce-doped $CaMnO_3$ requires more extreme conditions, reinforcing its strong preference for the oxidized state. Similar to Ti, this high structural and redox stability may limit the reactivity under typical operating conditions but could be advantageous for maintaining phase integrity and long-term performance in cyclic redox environments.

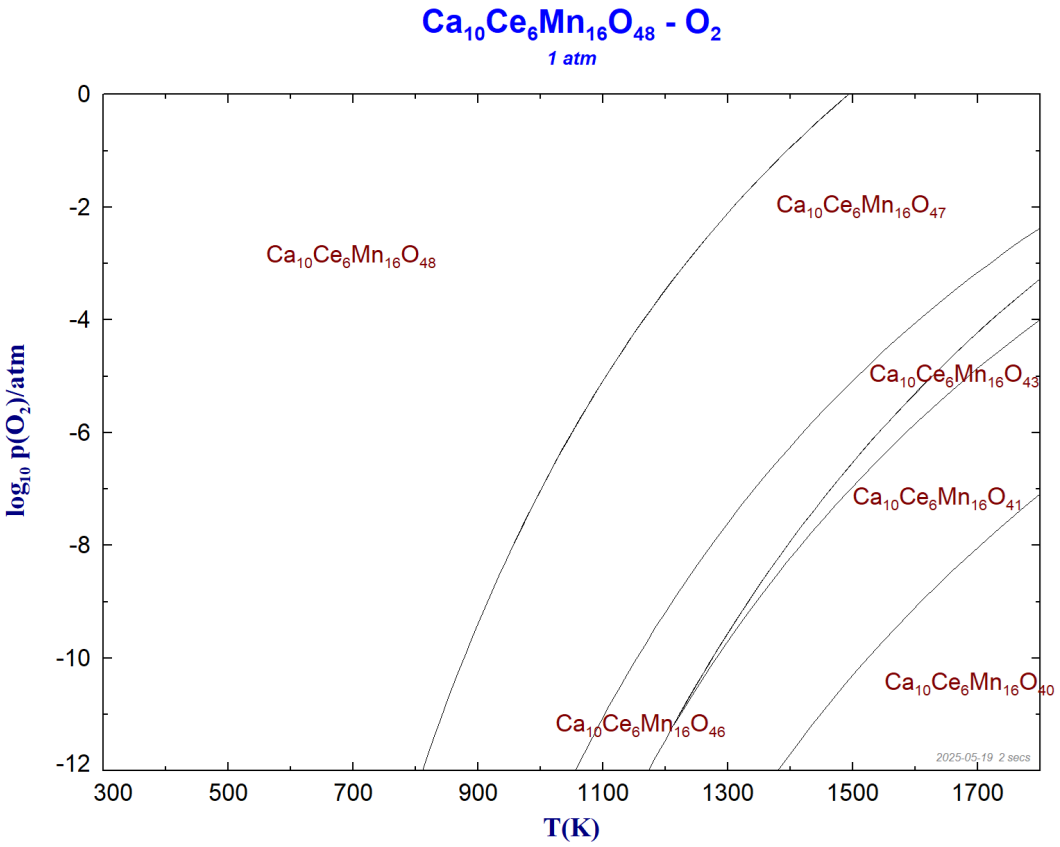

Figure 4.15: Phase stability diagram of Ce-doped $CaMnO_{3-\delta}$ as a function of temperature and oxygen partial pressure ($\log_{10} p(O_2)/\text{atm}$), calculated using FactSage.

4.5.5 La-doped $CaMnO_{3-\delta}$

The phase stability of La-doped $CaMnO_{3-\delta}$ (Figure 4.16) exhibits markedly different behavior compared to other dopants. In the intermediate temperature range of approximately 900–1300 K, the perovskite phase becomes completely unstable and decomposes into competing oxide phases containing Ca, Mn, and La, rather than forming a reduced $CaMnO_{3-\delta}$ phase. At higher temperatures, the system stabilizes again through the formation of reduced perovskite phases with oxygen vacancies. This breakdown behavior may arise from challenges in training the cluster expansion model for oxygen vacancies, where even a small increase in the formation enthalpy can tip the balance toward decomposition. However, experimental studies on La-doped $CaMnO_3$ [33] demonstrate its stability, suggesting that the present work underestimates the stability of $CaMnO_3$ with La-doping.

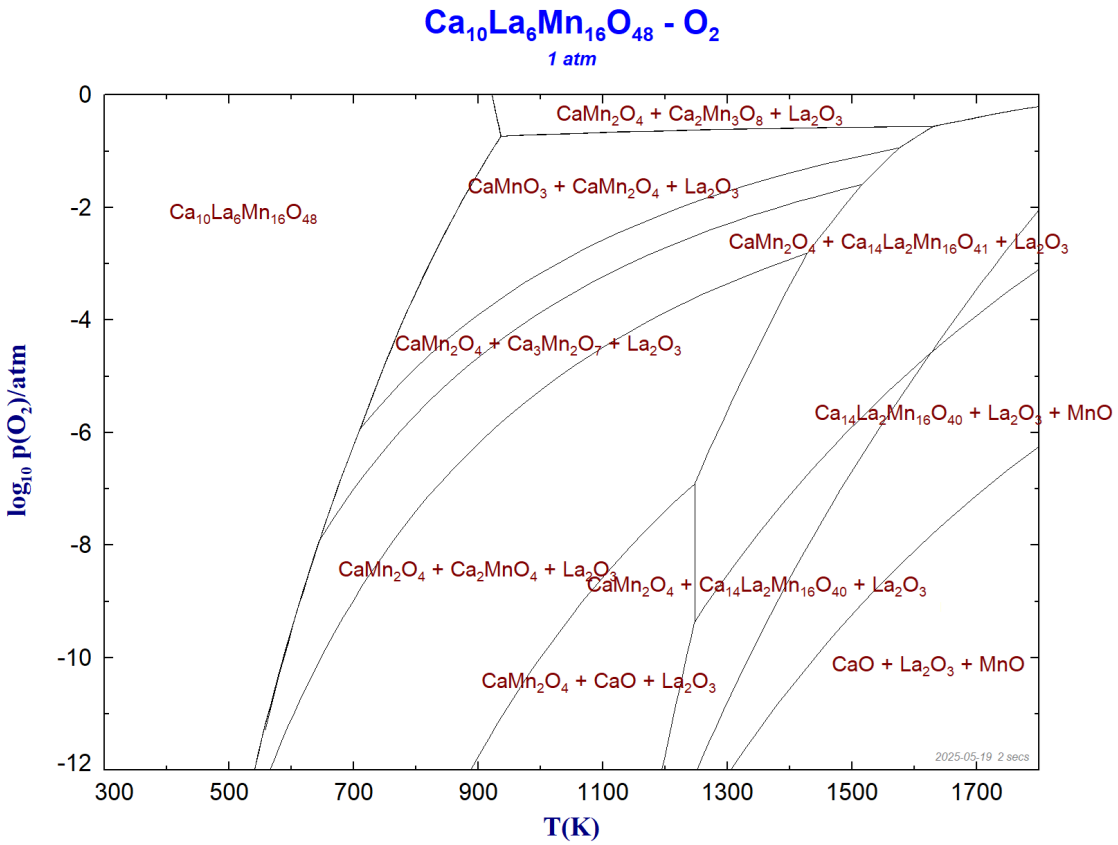

Figure 4.16: Phase stability diagram of La-doped $CaMnO_{3-\delta}$ as a function of temperature and oxygen partial pressure ($\log_{10} p(O_2)/\text{atm}$), calculated using FactSage.

4.5.6 Sr-doped $CaMnO_{3-\delta}$

The phase stability of Sr-doped $CaMnO_{3-\delta}$ (Figure 4.17) exhibits a gradual reduction across a broad range of temperatures and oxygen partial pressures. Unlike La doping, the perovskite phase remains stable under most conditions and reduces progressively with increasing temperature and decreasing $p(O_2)$. The decomposition into other oxide phases occurs only at very high temperatures, around 1700 K, and under strongly reducing conditions. Sr-doped $CaMnO_{3-\delta}$ shows reduction-oxidation behavior comparable to that of Fe-doped $CaMnO_3$. This indicates that Sr-doping gives a thermodynamic stable, redox-active perovskite potentially well-suited for CLC.

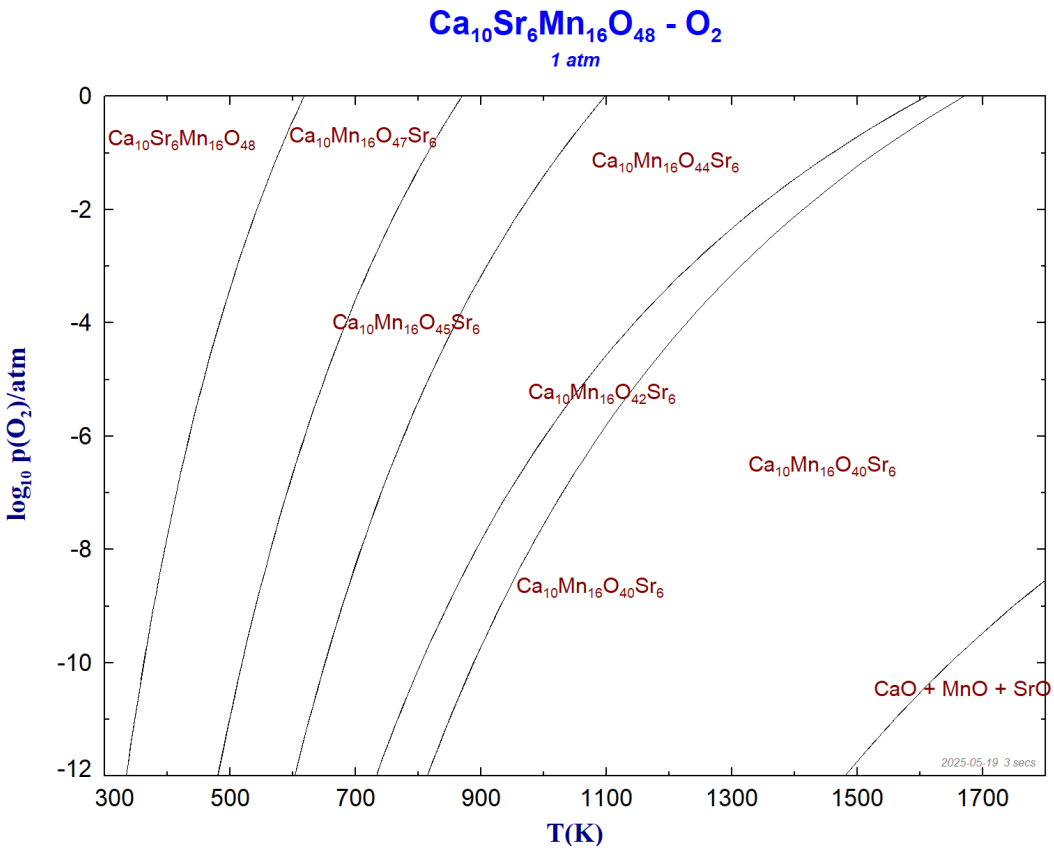

Figure 4.17: Phase stability diagram of Sr-doped $CaMnO_{3-\delta}$ as a function of temperature and oxygen partial pressure ($\log_{10} p(O_2)/\text{atm}$), calculated using FactSage.

4.6 Impact of Oxygen Vacancies on Cluster Expansion Accuracy

Inclusion of oxygen vacancies in cluster expansion for doped $CaMnO_3$ results in significantly higher root mean square error (RMSE) of the energy (eV / atom) and lower coefficient of determination (R^2) for both training and validation metrics compared to models without vacancies. As shown in Figure 4.18, the presence of oxygen vacancies leads to RMSE values that are at least an order of magnitude higher and R^2 values that are substantially lower than those for vacancy-free systems. This decline in accuracy is potentially due to the need to use shorter cutoffs, which could limit the model's ability to capture longer-range interactions.

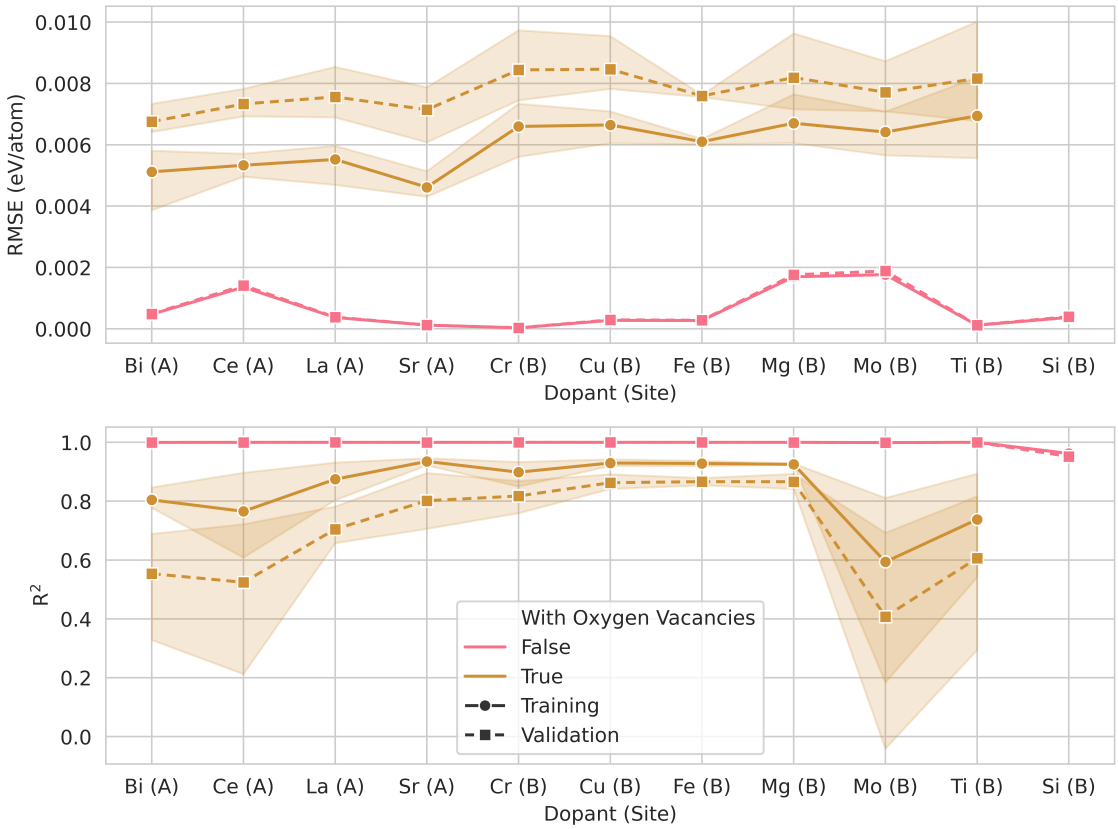

Figure 4.18: Comparison of RMSE and R^2 from CE training of doped $CaMnO_3$ with and without oxygen vacancies. Structures without oxygen vacancies (pink) exhibit significantly lower RMSE and R^2 values near unity compared to those with vacancies (brown).

A result of this inaccuracy in modeling oxygen vacancies could explain why some reduced phases did not appear in the phase diagrams for Mo, and why for La, they were right on the edge of stability.
Additionally, when comparing the configurational heat capacities, Ce-, Mo-, and Mg-doped systems exhibit greater disorder and lack the gradual shifts observed for other dopants (see Appendix A). These three dopants also show poorer CE (cluster expansion) training accuracy. This highlights the central role of CE in the methodology and demonstrates how even small fitting errors can lead to noticeable deviations in predicted thermodynamic behavior. It also suggests that CE-related inaccuracies are likely the largest source of error in this study.
An approach to reducing the CE training issue would involve a large increase in the size of the training data set and greater supercells.

4.7 Crystal Structure Stability of Doped $CaMnO_3$

Using the tolerance factor-based screening described in the Methods section, we evaluated the structural compatibility of a wide range of dopants across the periodic table. The goal was to identify elements that can substitute at the A- or B-site of

$CaMnO_3$ while maintaining a stable perovskite structure.

For A-site substitution, a preferred valence state of +2 and a coordination number of 12 are ideal. Although some Mn ions may adopt a Mn^{3+} valence state as a result of charge compensation, this possibility was not considered in this analysis and may be a small source of underestimation of the stability.

For B-site substitution, an ideal valence state of +4 and a coordination number of 6 are preferred. The following observations were made (see Figure 4.19):

- **Alkali metals** are unstable for A-sites and generally unstable for B-sites.
- **Alkaline earth metals** are just below the threshold for stability (i.e., stable) for both A- and B-sites, with the exception of Be.
- **Transition metals** generally appear to be stable for B-sites and mostly stable for A-sites, with exceptions such as V, Ni, and Cu.
- **Lanthanides and actinides** appear to be stable for both A- and B-sites.
- **Post-transition metals and others** show mixed stability depending on the specific element and site.

4.7.1 Periodic Table-Wide Trends

Figure 4.19 summarizes the computed tolerance factors for all screened elements. The color scale represents the tolerance factor values, while hatching denotes elements that exceed the stability threshold ($\tau = 4.18$). The probability of stability increases monotonically with decreasing Bartel tolerance factor τ [28]. Elements are divided into A- and B-site candidates: the A-site is represented by a large upward triangle in the left half of each cell, with smaller corner triangles indicating the absolute charge difference. The B-site is shown in the lower right half of each cell.

Note that the $\tau = 4.18$ threshold was originally trained on ABX_3 compounds and may therefore be less accurate for our doped structures than the reported 92% accuracy. However, it also achieves 91% accuracy on double perovskites $A_2B'BX_6$, which lie outside the original training set. This suggests that the model's performance is more dependent on composition than on structure [28].

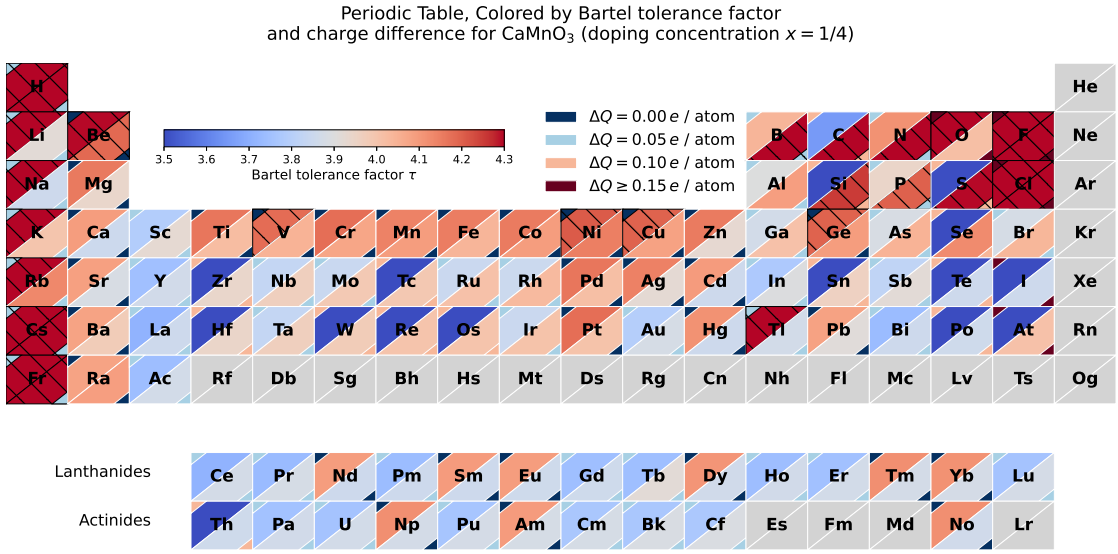

Figure 4.19: Bartel tolerance factors of most elements in the periodic table for doping in $CaMnO_3$, based on substitution at either the A-site or B-site. Hatches (diagonal lines) indicate a tolerance factor above the threshold of 4.18. Each element are divided into two sites, A-site for the upper left half, B-site for lower right. Additionally two small triangles in the corners that represent the absolute charge difference. Both color schemes go from blue to red, where blue is more favorable.

It is important to note that the analysis presented here is based on the cubic perovskite structure of $CaMnO_3$, while the thermodynamic calculations were performed for the orthorhombic phase. The choice of the cubic structure was motivated by the fact that applying the Bartel tolerance factor to the orthorhombic phase yielded unrealistic results, with nearly no stable dopants predicted. The primary structural difference between the cubic and orthorhombic phases lies in the coordination environment of the Ca ion: in the cubic phase, Ca has a coordination number (CN) of 12, whereas in the orthorhombic phase, it is 8. This significantly affects the ionic radius of Ca^{2+}, increasing from 1.12 Å (CN 8) to 1.34 Å (CN 12). The origin of the unrealistic results for the orthorhombic structure remains unclear, but it may be due to limitations or inconsistencies in the training data used for the threshold value.

5
Conclusion

Chemical-looping combustion and related technologies could be instrumental for achieving climate targets. One of the more interesting oxygen carriers is the perovskite $CaMnO_3$, which has shown a combination of high reactivity and reasonable stability during operation. Still, there are issues related to formation of irreversible phases during redox cycling which may limit its effectiveness. Further the effect of doping on material performance is not altogether understood. Hence, a broad computational study was employed in order to elucidate the effects of different dopants on the thermodynamics.

This work employed a comprehensive semi-empirical methodology to screen doped $CaMnO_3$ materials for chemical looping combustion. Ground states of doped structures with oxygen vacancies were estimated using cluster expansion models trained on structures relaxed by CHGNet, a machine learning interatomic potential. Vibrational contributions were included through phonon calculations with HiPhive and Phonopy, while configurational entropy was evaluated via Monte Carlo simulations. Final thermodynamic properties were refined using experimental data from NIST-JANAF and FactSage, enabling phase diagram construction and assessment of dopant effects on oxygen carrier stability.

A detailed phase diagram analysis of ten selected dopants, evaluated across a temperature range of 300 K to 1800 K and oxygen partial pressures from 1 atm to 10^{-12} atm, identified only four with favorable thermodynamic stability: Fe and Ti on the B-site, and Ce and Sr on the A-site. Most of the remaining dopants exhibited partial or complete instability, decomposing into secondary oxide phases. To improve agreement with the FactSage thermodynamic data, a correction of $-45\,\mathrm{kJ/mol}$ was applied to the formation enthalpies for the non-stoichiometric doped $CaMnO_3$ compounds.

Among the stable dopants, Fe and Sr had the ability to reduce at lower temperatures and higher p_{O_2}, while Ti and Ce offered greater structural stability under high-temperature and low-oxygen conditions.

The relatively high cluster expansion fitting error when oxygen vacancies were included in the compositions is very likely the largest source of error in the methodology. However, the formation enthalpies of Ti-doped $CaMnO_3$ with oxygen vacancies closely matched the values from FactSage computational data. This suggests that the impact of cluster expansion fitting inaccuracies on formation enthalpy may be limited, at least in the case of Ti doping. For La and Mo, the fitting error could have been enough to tip the scale toward instability, which warrants further study, especially since La doping has been shown to be stable experimentally [33]. Another source of error arises from the use of the machine learning potential (CHGNet) instead of direct DFT calculations; however, the close agreement with Gastaldi *et*

al. [12] indicates that CHGNet is a suitable substitute for DFT.
A limitation of this study is the exclusive use of orthorhombic $CaMnO_3$ structures to estimate thermodynamic properties. Future research exploring the cubic phase may offer deeper insight into the predicted instability of certain dopants.
In general, the combination of tolerance factor screening, phase stability analysis, and validation against external data provides a robust framework for identifying stable dopants while also highlighting the sensitivities of current modeling approaches when dealing with complex defect structures.

Key Findings:

- **Thermodynamic data of doped $CaMnO_3$:** Cr, Cu, Fe, Mg, Mo, Si, Ti (B-site); Bi, Ce, La, Sr (A-site).
- **Promising dopants:** Fe, Ti (B-site); Ce, Sr (A-site).
- **Reduction behavior:** Fe and Sr reduce at higher oxygen partial pressures, lower temperatures, and improve stability over pristine $CaMnO_3$, while Ti and Ce offer even greater thermal and chemical stability.
- **Stability validation:** The formation enthalpies of Ti-doped $CaMnO_3$, across varying doping concentrations and oxygen vacancy levels, agree with the FactSage computational data despite inaccuracies in the cluster expansion training.
- **Modeling insight:** Framework is generally effective but potentially sensitive to vacancy-induced cluster expansion errors.

Bibliography

[1] IPCC, "The ipcc special report on carbon dioxide capture and storage," 2005.

[2] N. Pour, P. A. Webley, and P. J. Cook, "A sustainability framework for bioenergy with carbon capture and storage (beccs) technologies," vol. 114, p. 6044 – 6056, 2017. Cited by: 31; All Open Access, Gold Open Access.

[3] *The potential for carbon sequestration in the United States*. 2013. Cited by: 0.

[4] C. Linderholm, M. Schmitz, M. Biermann, M. Hanning, and A. Lyngfelt, "Chemical-looping combustion of solid fuel in a 100 kw unit using sintered manganese ore as oxygen carrier," *International Journal of Greenhouse Gas Control*, vol. 65, p. 170 – 181, 2017. Cited by: 63.

[5] A. Lyngfelt, "20 - chemical looping combustion (clc)," in *Fluidized Bed Technologies for Near-Zero Emission Combustion and Gasification* (F. Scala, ed.), Woodhead Publishing Series in Energy, pp. 895–930, Woodhead Publishing, 2013.

[6] J. Adanez, A. Abad, F. Garcia-Labiano, P. Gayan, and L. F. De Diego, "Progress in chemical-looping combustion and reforming technologies," *Progress in Energy and Combustion Science*, vol. 38, no. 2, p. 215 – 282, 2012. Cited by: 2110.

[7] N. Galinsky, M. Sendi, L. Bowers, and F. Li, "Camn1xbxo3 (b=al, v, fe, co, and ni) perovskite based oxygen carriers for chemical looping with oxygen uncoupling (clou)," *Applied Energy*, vol. 174, pp. 80–87, 2016.

[8] M. Pishahang, Y. Larring, M. Sunding, M. Jacobs, and F. Snijkers, "Performance of perovskite-type oxides as oxygen-carrier materials for chemical looping combustion in the presence of h2s," *Energy Technology*, vol. 4, no. 10, pp. 1305–1316, 2016.

[9] Z. Miao, L. Shen, Z. Li, and T. Shen, "Sintering and agglomeration characteristics of industrially prepared camn0.5ti0.375fe0.125o3- perovskite oxygen carrier in chemical looping combustion," *Chemical Engineering Journal*, vol. 472, p. 144722, 2023.

[10] X. Yin, S. Wang, B. Wang, and L. Shen, "Perovskite-type lamn1xbxo3+ (b = fe, co and ni) as oxygen carriers for chemical looping steam methane reforming," *Chemical Engineering Journal*, vol. 422, p. 128751, 2021.

[11] A. Cabello, A. Abad, P. Gayán, F. García-Labiano, L. F. de Diego, and J. Adánez, "Increasing energy efficiency in chemical looping combustion of methane by in-situ activation of perovskite-based oxygen carriers," *Applied Energy*, vol. 287, p. 116557, 2021.

[12] J. Gastaldi, J. Brorsson, I. Staničić, A. Hellman, and T. Mattisson, "First-principles estimation of thermodynamic properties and phase stability of

camno3 for chemical-looping combustion," *Energy & Fuels*, vol. 0, no. 0, p. null, 0.

[13] Q. Zhou and B. J. Kennedy, "Thermal expansion and structure of orthorhombic camno3," *Journal of Physics and Chemistry of Solids*, vol. 67, no. 7, pp. 1595–1598, 2006.

[14] T. Mattisson, M. Keller, C. Linderholm, P. Moldenhauer, M. Rydén, H. Leion, and A. Lyngfelt, "Chemical-looping technologies using circulating fluidized bed systems: Status of development," *Fuel Processing Technology*, vol. 172, pp. 1–12, 2018.

[15] H. Fang, L. Haibin, and Z. Zengli, "Advancements in development of chemical-looping combustion: A review," *International Journal of Chemical Engineering*, vol. 2009, no. 1, p. 710515, 2009.

[16] J. Adánez and A. Abad, "Chemical-looping combustion: Status and research needs," *Proceedings of the Combustion Institute*, vol. 37, no. 4, pp. 4303–4317, 2019.

[17] B. Deng, P. Zhong, K. Jun, J. Riebesell, K. Han, C. J. Bartel, and G. Ceder, "Chgnet as a pretrained universal neural network potential for charge-informed atomistic modelling," *Nature Machine Intelligence*, 2023.

[18] M. Ångqvist, W. A. Muñoz, J. M. Rahm, E. Fransson, C. Durniak, P. Rozyczko, T. H. Rod, and P. Erhart, "Icet – a python library for constructing and sampling alloy cluster expansions," *Advanced Theory and Simulations*, vol. 2, no. 7, p. 1900015, 2019.

[19] A. Togo, "First-principles phonon calculations with phonopy and phono3py," *J. Phys. Soc. Jpn.*, vol. 92, no. 1, p. 012001, 2023.

[20] J. Brorsson, I. Staničić, J. Gastaldi, T. Mattison, and A. Hellman, "Thermodynamic properties for metal oxides from first-principles," *Computational Materials Science*, vol. 233, p. 112690, 2024.

[21] A. Benisek and E. Dachs, "The accuracy of standard enthalpies and entropies for phases of petrological interest derived from density-functional calculations," *Contributions to Mineralogy and Petrology*, vol. 173, no. 11, p. 90, 2018.

[22] A. Jain, S. P. Ong, G. Hautier, W. Chen, W. D. Richards, S. Dacek, S. Cholia, D. Gunter, D. Skinner, G. Ceder, and K. A. Persson, "Commentary: The materials project: A materials genome approach to accelerating materials innovation," *APL Materials*, vol. 1, p. 011002, 07 2013.

[23] F. Eriksson, E. Fransson, and P. Erhart, "The hiphive package for the extraction of high-order force constants by machine learning," *Advanced Theory and Simulations*, vol. 2, no. 5, p. 1800184, 2019.

[24] A. Togo, L. Chaput, T. Tadano, and I. Tanaka, "Implementation strategies in phonopy and phono3py," *J. Phys. Condens. Matter*, vol. 35, no. 35, p. 353001, 2023.

[25] C. W. Bale, E. Bélisle, P. Chartrand, S. A. Decterov, G. Eriksson, A. E. Gheribi, K. Hack, I. H. Jung, Y. B. Kang, J. Melançon, A. D. Pelton, S. Petersen, C. Robelin, J. Sangster, P. Spencer, and M.-A. Van Ende, "FactSage thermochemical software and databases – 2010–2016," *Calphad*, vol. 54, pp. 35–53, 2016.

[26] K. T. Jacob, A. Kumar, G. Rajitha, and Y. Waseda, "Thermodynamic data for mn3o4, mn2o3 and mno2," *High Temperature Materials and Processes*, vol. 30, no. 4, pp. 459–472, 2011.

[27] K. T. Jacob, A. Kumar, and Y. Waseda, "Gibbs energy of formation of mno: Measurement and assessment," *Journal of Phase Equilibria and Diffusion*, vol. 29, no. 3, pp. 222–230, 2008.

[28] C. J. Bartel, C. Sutton, B. R. Goldsmith, R. Ouyang, C. B. Musgrave, L. M. Ghiringhelli, and M. Scheffler, "New tolerance factor to predict the stability of perovskite oxides and halides," *Science Advances*, vol. 5, no. 2, p. eaav0693, 2019.

[29] R. D. Shannon, "Revised effective ionic radii and systematic studies of interatomic distances in halides and chalcogenides," *Acta Crystallographica Section A*, vol. 32, pp. 751–767, Sep 1976.

[30] A. Benisek and E. Dachs, "The vibrational and configurational entropy of disordering in cu_3au," *Journal of Alloys and Compounds*, vol. 632, pp. 585–590, May 2015.

[31] E. Bakken, J. Boerio-Goates, T. Grande, B. Hovde, T. Norby, L. Rørmark, R. Stevens, and S. Stølen, "Entropy of oxidation and redox energetics of camno3," *Solid State Ionics*, vol. 176, no. 29, pp. 2261–2267, 2005.

[32] M. Rydén, A. Lyngfelt, and T. Mattisson, "Camn0.875ti0.125o3 as oxygen carrier for chemical-looping combustion with oxygen uncoupling (clou)—experiments in a continuously operating fluidized-bed reactor system," *International Journal of Greenhouse Gas Control*, vol. 5, no. 2, pp. 356–366, 2011.

[33] M. Arjmand, A. Hedayati, A.-M. Azad, H. Leion, M. Rydén, and T. Mattisson, "Caxla1–xmn1–ymyo3 (m = mg, ti, fe, or cu) as oxygen carriers for chemical-looping with oxygen uncoupling (clou)," *Energy & Fuels*, vol. 27, no. 8, pp. 4097–4107, 2013.

A

Figures

A.1 Configurational and Reaction Heat Capacity

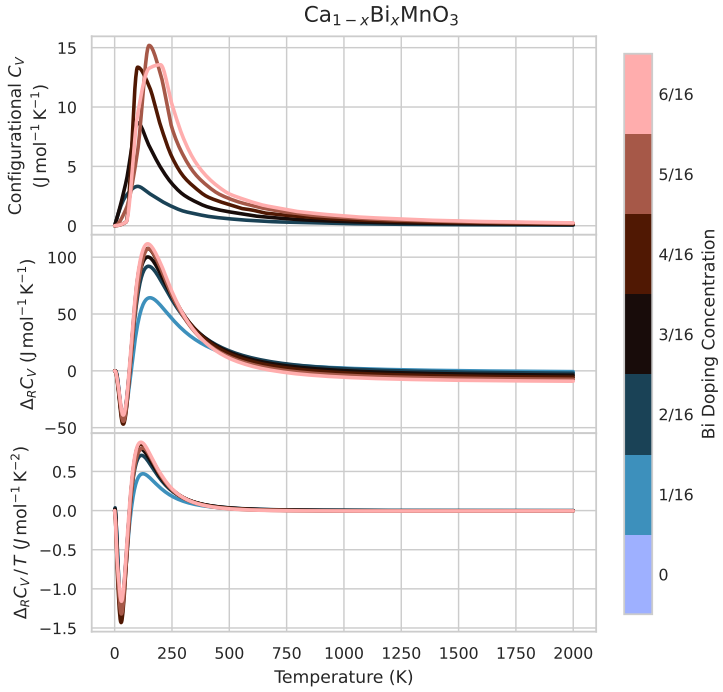

Figure A.1: Reaction heat capacity $\Delta_R C_V$, $\Delta_R C_V/T$, and configurational heat capacity C_V for Bi-doped $CaMnO_3$.

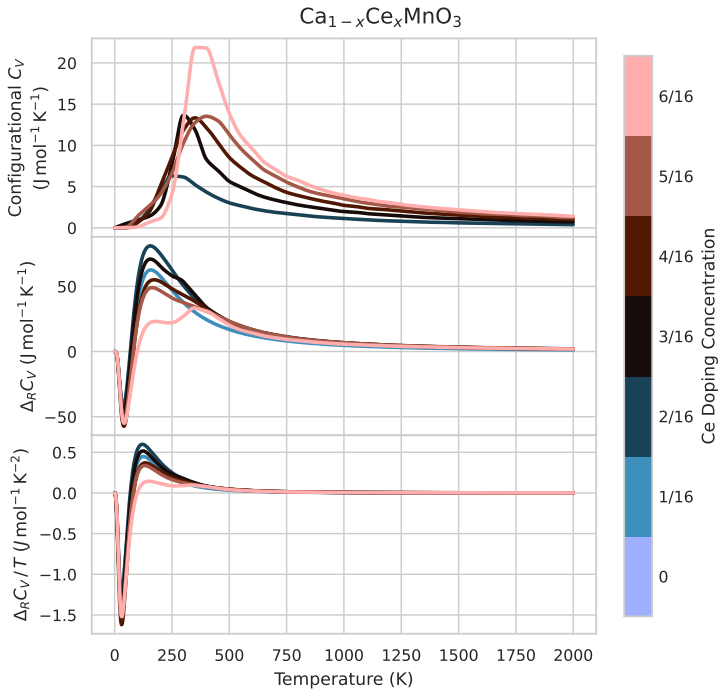

Figure A.2: Reaction heat capacity $\Delta_R C_V$, $\Delta_R C_V/T$, and configurational heat capacity C_V for Ce-doped $CaMnO_3$.

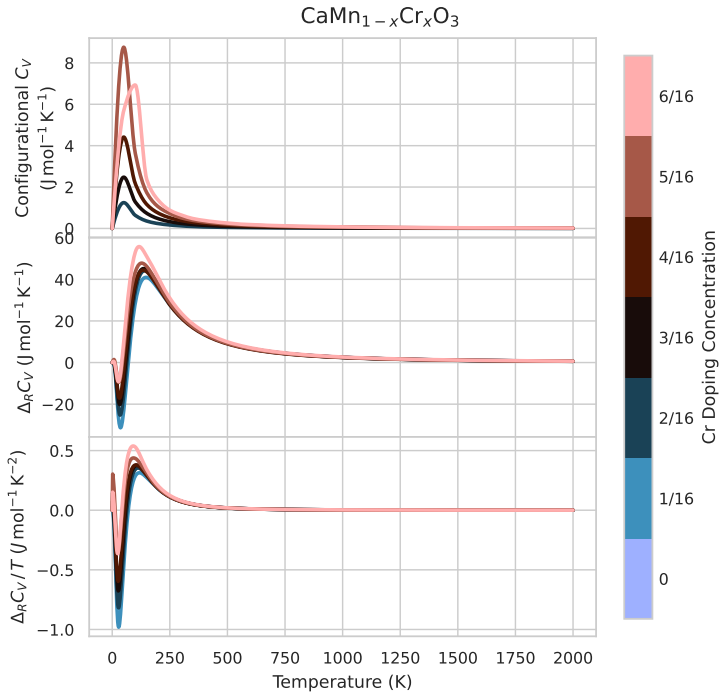

Figure A.3: Reaction heat capacity $\Delta_R C_V$, $\Delta_R C_V/T$, and configurational heat capacity C_V for Cr-doped $CaMnO_3$.

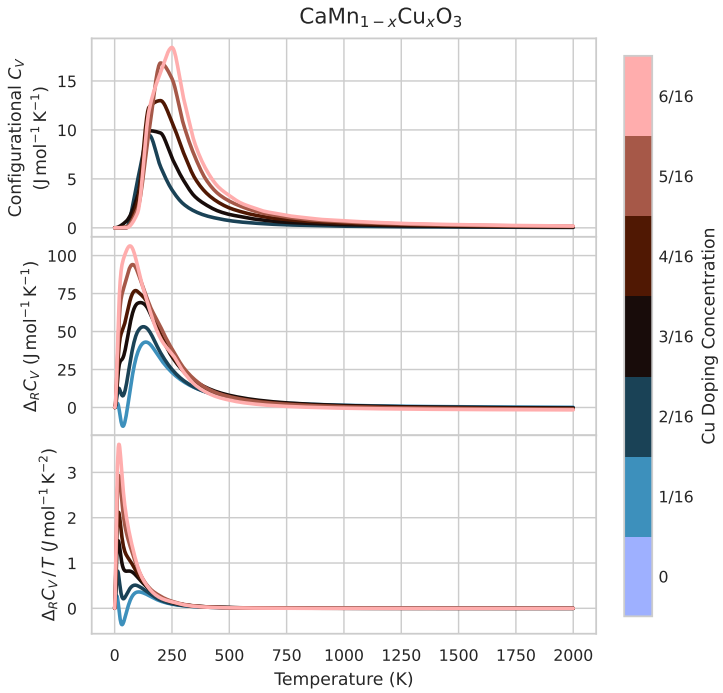

Figure A.4: Reaction heat capacity $\Delta_R C_V$, $\Delta_R C_V/T$, and configurational heat capacity C_V for Cu-doped $CaMnO_3$.

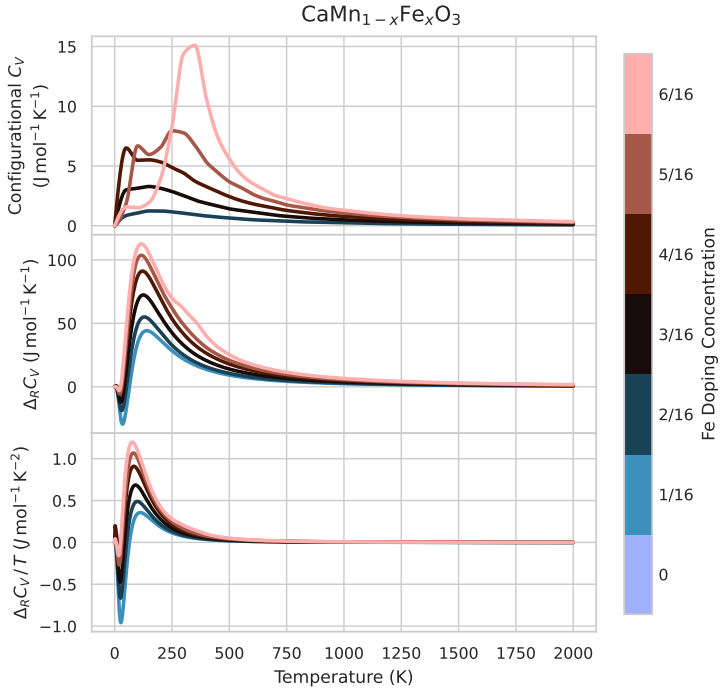

Figure A.5: Reaction heat capacity $\Delta_R C_V$, $\Delta_R C_V/T$, and configurational heat capacity C_V for Fe-doped $CaMnO_3$.

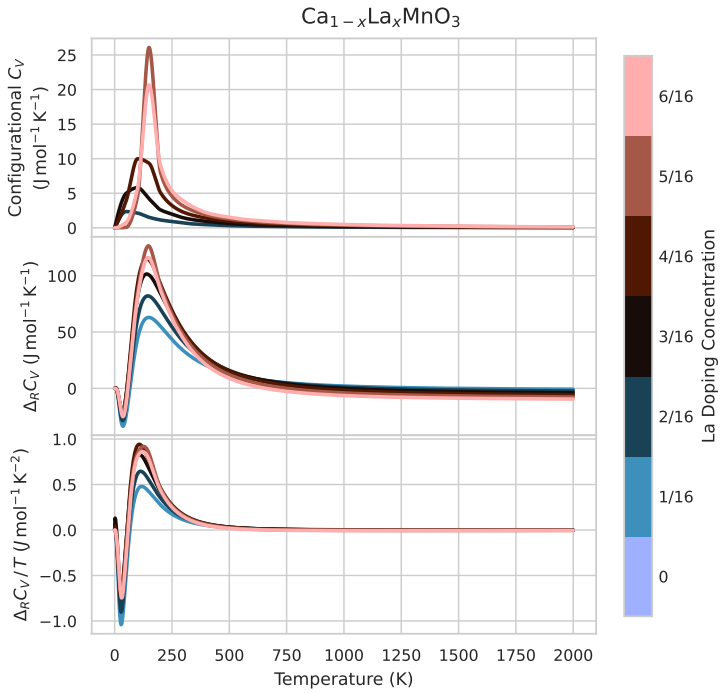

Figure A.6: Reaction heat capacity $\Delta_R C_V$, $\Delta_R C_V/T$, and configurational heat capacity C_V for La-doped $CaMnO_3$.

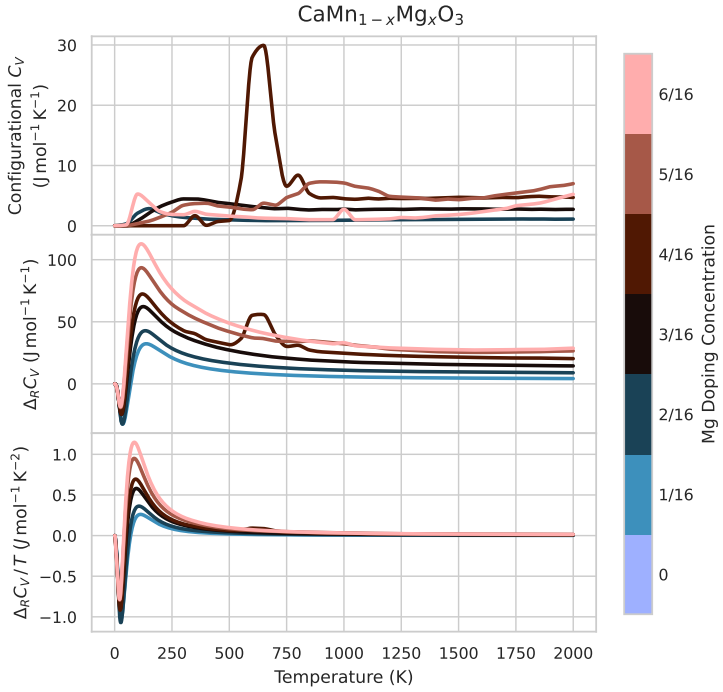

Figure A.7: Reaction heat capacity $\Delta_R C_V$, $\Delta_R C_V/T$, and configurational heat capacity C_V for Mg-doped $CaMnO_3$.

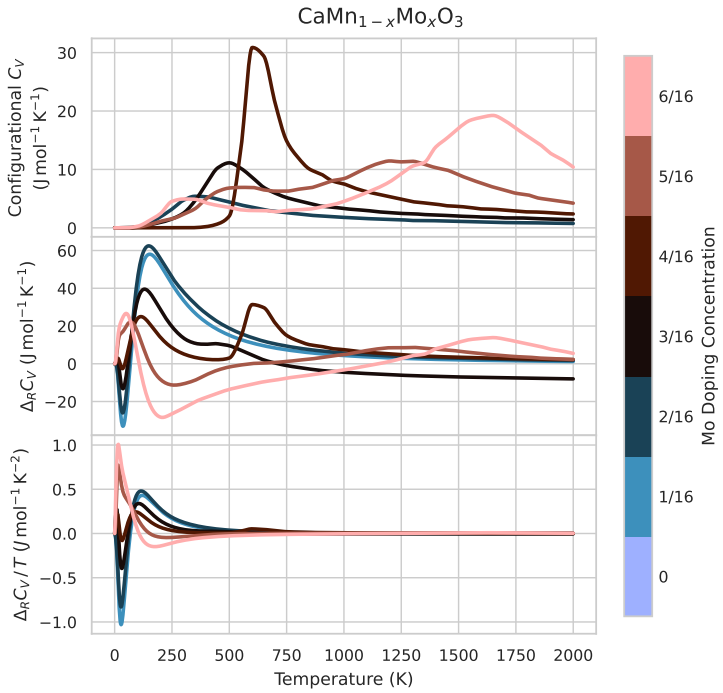

Figure A.8: Reaction heat capacity $\Delta_R C_V$, $\Delta_R C_V/T$, and configurational heat capacity C_V for Mo-doped $CaMnO_3$.

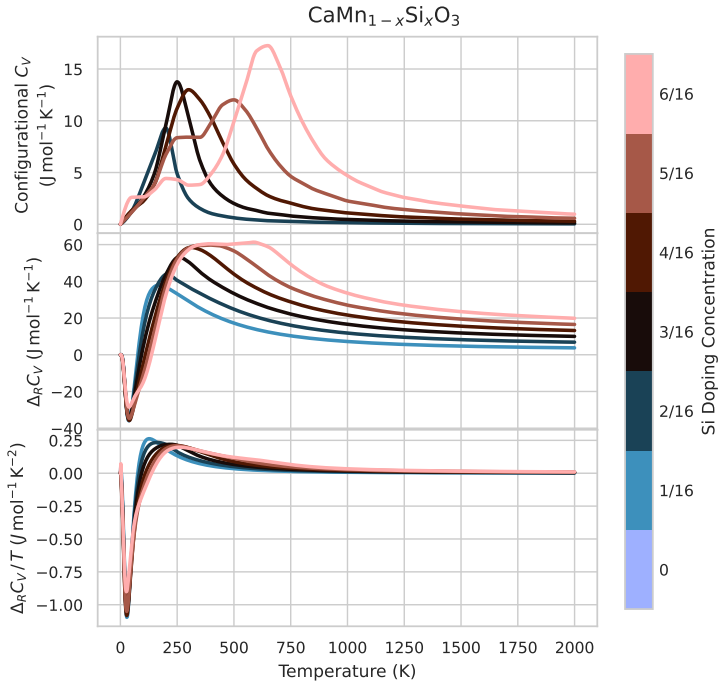

Figure A.9: Reaction heat capacity $\Delta_R C_V$, $\Delta_R C_V/T$, and configurational heat capacity C_V for Si-doped $CaMnO_3$.

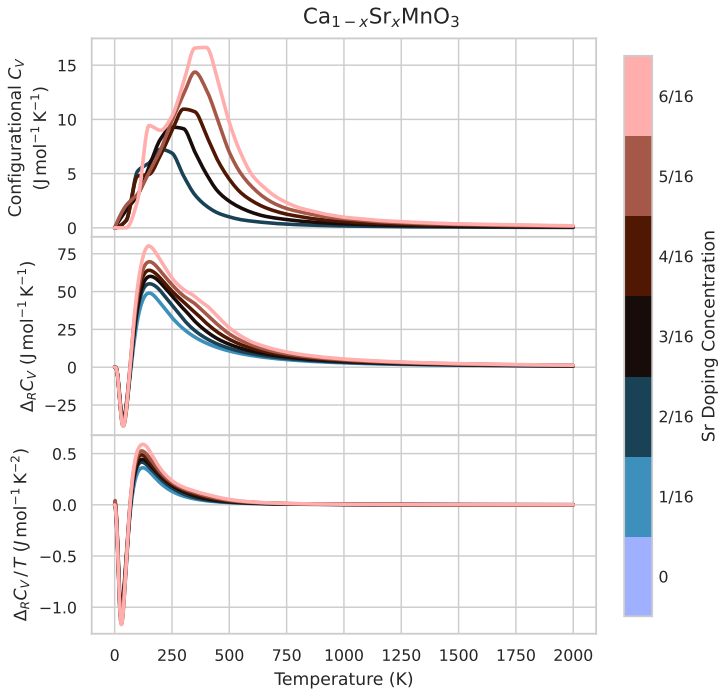

Figure A.10: Reaction heat capacity $\Delta_R C_V$, $\Delta_R C_V/T$, and configurational heat capacity C_V for Sr-doped $CaMnO_3$.

B

Tables

B.1 Thermodynamic Data

Thermodynamic data for doped CaMnO3 with entropy S in J/(mol K), formation enthalpy ΔH_f in kJ/mol and parameters for heat capacity with function $C_P(T) = k_0 + k_1 T^{-2} + k_2 T^{-0.5} + k_3 T^{-3}$. Note that the formation enthalpy is after the correction for the FactSage phase diagrams (-720 kJ/mol).

Table B.1: Thermodynamic parameters for Bi, Ce, Cr, Cu, and Fe-doped $CaMnO_3$. Entropy S in J/(mol K), enthalpy ΔH_f in kJ/mol.

Compound	ΔH_f	S	k_0	k_1	k_2	k_3
$BiCa_{15}Mn_{16}O_{48}$	-1.93992×10^7	1377	3832	2.13596×10^8	-5.58610×10^4	-3.95016×10^{10}
$Bi_2Ca_{14}Mn_{16}O_{48}$	-1.89934×10^7	1398	3894	2.28238×10^8	-5.80230×10^4	-4.16303×10^{10}
$Bi_3Ca_{13}Mn_{16}O_{48}$	-1.85890×10^7	1390	3956	2.41229×10^8	-6.01650×10^4	-4.35709×10^{10}
$Bi_4Ca_{12}Mn_{16}O_{48}$	-1.81797×10^7	1375	4017	2.54098×10^8	-6.23080×10^4	-4.54923×10^{10}
$Bi_5Ca_{11}Mn_{16}O_{48}$	-1.77580×10^7	1359	4079	2.66442×10^8	-6.44400×10^4	-4.73346×10^{10}
$Bi_6Ca_{10}Mn_{16}O_{48}$	-1.73308×10^7	1362	4141	2.79300×10^8	-6.65840×10^4	-4.92337×10^{10}
$Ca_{15}CeMn_{16}O_{48}$	-2.02069×10^7	1442	3018	-6.44884×10^7	-2.26110×10^4	1.61016×10^{10}
$Ca_{14}Ce_2Mn_{16}O_{48}$	-2.06020×10^7	1514	3055	-6.08684×10^7	-2.33260×10^4	1.59365×10^{10}
$Ca_{13}Ce_3Mn_{16}O_{48}$	-2.09792×10^7	1547	3091	-5.93495×10^7	-2.40130×10^4	1.61210×10^{10}
$Ca_{12}Ce_4Mn_{16}O_{48}$	-2.13444×10^7	1562	3133	-5.34530×10^7	-2.50120×10^4	1.49118×10^{10}
$Ca_{11}Ce_5Mn_{16}O_{48}$	-2.16811×10^7	1612	3172	-4.91650×10^7	-2.58360×10^4	1.41027×10^{10}
$Ca_{10}Ce_6Mn_{16}O_{48}$	-2.20161×10^7	1627	3220	-4.18298×10^7	-2.71210×10^4	1.28427×10^{10}
$Ca_{16}CrMn_{15}O_{48}$	-1.93644×10^7	1603	2926	-6.38472×10^7	-2.12050×10^4	1.50051×10^{10}
$Ca_{16}Cr_2Mn_{14}O_{48}$	-1.89331×10^7	1838	2870	-5.84546×10^7	-2.05190×10^4	1.35074×10^{10}
$Ca_{16}Cr_3Mn_{13}O_{48}$	-1.85017×10^7	2070	2814	-5.31903×10^7	-1.98330×10^4	1.20209×10^{10}
$Ca_{16}Cr_4Mn_{12}O_{48}$	-1.80705×10^7	2297	2758	-4.79872×10^7	-1.91470×10^4	1.05366×10^{10}
$Ca_{16}Cr_5Mn_{11}O_{48}$	-1.76377×10^7	2538	2702	-4.25937×10^7	-1.84610×10^4	9.03515×10^9
$Ca_{16}Cr_6Mn_{10}O_{48}$	-1.72045×10^7	2768	2646	-3.70486×10^7	-1.77760×10^4	7.51883×10^9
$Ca_{16}CuMn_{15}O_{48}$	-1.94034×10^7	1404	3635	1.63244×10^8	-4.86050×10^4	-3.06958×10^{10}
$Ca_{16}Cu_2Mn_{14}O_{48}$	-1.90100×10^7	1438	3502	1.28999×10^8	-4.35260×10^4	-2.42441×10^{10}
$Ca_{16}Cu_3Mn_{13}O_{48}$	-1.86031×10^7	1487	3368	9.52322×10^7	-3.84350×10^4	-1.78061×10^{10}
$Ca_{16}Cu_4Mn_{12}O_{48}$	-1.82046×10^7	1513	3234	6.05226×10^7	-3.33400×10^4	-1.12440×10^{10}
$Ca_{16}Cu_5Mn_{11}O_{48}$	-1.78031×10^7	1553	3100	2.62215×10^7	-2.82630×10^4	-4.72847×10^9
$Ca_{16}Cu_6Mn_{10}O_{48}$	-1.74116×10^7	1572	2966	-9.05179×10^6	-2.31580×10^4	1.90637×10^9
$Ca_{16}FeMn_{15}O_{48}$	-1.97623×10^7	1368	3323	6.51365×10^7	-3.59310×10^4	-1.23370×10^{10}
$Ca_{16}Fe_2Mn_{14}O_{48}$	-1.97259×10^7	1379	3075	-3.18659×10^6	-2.60690×10^4	-2.58546×10^8
$Ca_{16}Fe_3Mn_{13}O_{48}$	-1.96824×10^7	1394	2827	-7.07512×10^7	-1.62120×10^4	1.17182×10^{10}
$Ca_{16}Fe_4Mn_{12}O_{48}$	-1.96370×10^7	1415	2580	-1.38004×10^8	-6.36900×10^3	2.36462×10^{10}
$Ca_{16}Fe_5Mn_{11}O_{48}$	-1.95958×10^7	1412	2333	-2.05484×10^8	3.44700×10^3	3.56392×10^{10}
$Ca_{16}Fe_6Mn_{10}O_{48}$	-1.95500×10^7	1415	2092	-2.70103×10^8	1.29840×10^4	4.72301×10^{10}

Table B.2: Thermodynamic parameters for La, Mg, Mo, and Si-doped $CaMnO_3$. Entropy S in J/(mol K), enthalpy ΔH_f in kJ/mol.

Compound	ΔH_f	S	k_0	k_1	k_2	k_3
$Ca_{15}LaMn_{16}O_{48}$	-2.00319×10^7	1378	2988	-6.94354×10^7	-2.19890×10^4	1.71350×10^{10}
$Ca_{14}La_2Mn_{16}O_{48}$	-2.02680×10^7	1384	2994	-7.04623×10^7	-2.20820×10^4	1.78838×10^{10}
$Ca_{13}La_3Mn_{16}O_{48}$	-2.04969×10^7	1394	3000	-7.17646×10^7	-2.21700×10^4	1.86783×10^{10}
$Ca_{12}La_4Mn_{16}O_{48}$	-2.07282×10^7	1379	3006	-7.36428×10^7	-2.22530×10^4	1.95358×10^{10}
$Ca_{11}La_5Mn_{16}O_{48}$	-2.09586×10^7	1350	3012	-7.64707×10^7	-2.23270×10^4	2.04978×10^{10}
$Ca_{10}La_6Mn_{16}O_{48}$	-2.11984×10^7	1314	3018	-7.93608×10^7	-2.23960×10^4	2.14731×10^{10}
$Ca_{16}MgMn_{15}O_{48}$	-1.98880×10^7	1453	2957	-6.04094×10^7	-2.17340×10^4	1.39759×10^{10}
$Ca_{16}Mg_2Mn_{14}O_{48}$	-1.99627×10^7	1550	2934	-4.95960×10^7	-2.16230×10^4	1.11745×10^{10}
$Ca_{16}Mg_3Mn_{13}O_{48}$	-1.99990×10^7	1673	2911	-3.73096×10^7	-2.15320×10^4	8.11993×10^9
$Ca_{16}Mg_4Mn_{12}O_{48}$	-2.00285×10^7	1770	2851	-3.58512×10^7	-1.98350×10^4	6.42925×10^9
$Ca_{16}Mg_5Mn_{11}O_{48}$	-2.00368×10^7	1894	2849	-2.28170×10^7	-2.05690×10^4	4.11333×10^9
$Ca_{16}Mg_6Mn_{10}O_{48}$	-2.00367×10^7	2003	2842	-1.31267×10^6	-2.13750×10^4	-8.99360×10^8
$Ca_{16}Mn_{15}MoO_{48}$	-2.00557×10^7	1397	3057	-3.29754×10^7	-2.52520×10^4	8.92764×10^9
$Ca_{16}Mn_{14}Mo_2O_{48}$	-2.03004×10^7	1412	3135	3.47557×10^6	-2.86890×10^4	1.14483×10^9
$Ca_{16}Mn_{13}Mo_3O_{48}$	-2.05380×10^7	1405	3204	4.17081×10^7	-3.22540×10^4	-7.65468×10^9
$Ca_{16}Mn_{12}Mo_4O_{48}$	-2.07699×10^7	1398	3217	4.40059×10^7	-3.23180×10^4	-9.07872×10^9
$Ca_{16}Mn_{11}Mo_5O_{48}$	-2.09676×10^7	1405	3360	9.14090×10^7	-3.83610×10^4	-1.82289×10^{10}
$Ca_{16}Mn_{10}Mo_6O_{48}$	-2.11566×10^7	1393	3524	1.52794×10^8	-4.54730×10^4	-3.07200×10^{10}
$Ca_{16}Mn_{15}O_{48}Si$	-2.01209×10^7	1374	2926	-7.21268×10^7	-2.03360×10^4	1.58730×10^{10}
$Ca_{16}Mn_{14}O_{48}Si_2$	-2.04516×10^7	1375	2870	-7.55857×10^7	-1.87640×10^4	1.53789×10^{10}
$Ca_{16}Mn_{13}O_{48}Si_3$	-2.07865×10^7	1372	2813	-7.99713×10^7	-1.71270×10^4	1.52699×10^{10}
$Ca_{16}Mn_{12}O_{48}Si_4$	-2.11265×10^7	1364	2766	-7.70411×10^7	-1.60000×10^4	1.33255×10^{10}
$Ca_{16}Mn_{11}O_{48}Si_5$	-2.14677×10^7	1361	2709	-7.64356×10^7	-1.44030×10^4	1.12725×10^{10}
$Ca_{16}Mn_{10}O_{48}Si_6$	-2.18133×10^7	1365	2612	-9.63066×10^7	-1.09750×10^4	1.36641×10^{10}

Table B.3: Thermodynamic parameters for Sr, and Ti-doped $CaMnO_3$. Entropy S in J/(mol K), enthalpy ΔH_f in kJ/mol.

Compound	ΔH_f	S	k_0	k_1	k_2	k_3
$Ca_{15}Mn_{16}O_{48}Sr$	-1.97625×10^7	1399	3005	-6.21970×10^7	-2.27310×10^4	1.53468×10^{10}
$Ca_{14}Mn_{16}O_{48}Sr_2$	-1.97352×10^7	1427	3027	-5.55365×10^7	-2.35580×10^4	1.43428×10^{10}
$Ca_{13}Mn_{16}O_{48}Sr_3$	-1.97123×10^7	1454	3052	-4.75182×10^7	-2.44830×10^4	1.30694×10^{10}
$Ca_{12}Mn_{16}O_{48}Sr_4$	-1.96953×10^7	1471	3080	-3.67992×10^7	-2.55930×10^4	1.10950×10^{10}
$Ca_{11}Mn_{16}O_{48}Sr_5$	-1.96730×10^7	1498	3111	-2.49033×10^7	-2.67900×10^4	8.83199×10^9
$Ca_{10}Mn_{16}O_{48}Sr_6$	-1.96544×10^7	1521	3141	-1.28385×10^7	-2.79820×10^4	6.49871×10^9
$Ca_{16}Mn_{15}O_{48}Ti$	-2.02751×10^7	1396	2954	-6.24166×10^7	-2.13120×10^4	1.44025×10^{10}
$Ca_{16}Mn_{14}O_{48}Ti_2$	-2.07571×10^7	1419	2927	-5.58694×10^7	-2.07190×10^4	1.23111×10^{10}
$Ca_{16}Mn_{13}O_{48}Ti_3$	-2.12413×10^7	1443	2898	-4.92462×10^7	-2.01080×10^4	1.01648×10^{10}
$Ca_{16}Mn_{12}O_{48}Ti_4$	-2.17269×10^7	1451	2870	-4.13908×10^7	-1.94970×10^4	7.58764×10^9
$Ca_{16}Mn_{11}O_{48}Ti_5$	-2.22112×10^7	1461	2821	-4.22828×10^7	-1.79840×10^4	6.60714×10^9
$Ca_{16}Mn_{10}O_{48}Ti_6$	-2.26986×10^7	1459	2743	-5.92427×10^7	-1.50680×10^4	9.22191×10^9

Table B.4: Thermodynamic parameters for Bi-doped $CaMnO_3$ with varying oxygen vacancy concentration. Entropy S in J/(mol K), enthalpy ΔH_f in kJ/mol.

Compound	ΔH_f	S	k_0	k_1	k_2	k_3
$Bi_2Ca_{14}Mn_{16}O_{47}$	-1.88572×10^7	1445	3699	2.13435×10^8	-5.19420×10^4	-4.19189×10^{10}
$Bi_2Ca_{14}Mn_{16}O_{46}$	-1.87135×10^7	1463	3471	1.63266×10^8	-4.37460×10^4	-3.39642×10^{10}
$Bi_2Ca_{14}Mn_{16}O_{45}$	-1.85760×10^7	1451	3198	6.18933×10^7	-3.28850×10^4	-1.28328×10^{10}
$Bi_2Ca_{14}Mn_{16}O_{44}$	-1.83875×10^7	1481	3124	4.01821×10^7	-3.06060×10^4	-7.93568×10^9
$Bi_2Ca_{14}Mn_{16}O_{43}$	-1.82072×10^7	1494	3078	3.79368×10^7	-3.01270×10^4	-7.39432×10^9
$Bi_2Ca_{14}Mn_{16}O_{42}$	-1.80812×10^7	1497	3052	3.77972×10^7	-2.98380×10^4	-7.43085×10^9
$Bi_2Ca_{14}Mn_{16}O_{41}$	-1.78614×10^7	1486	3066	6.97507×10^7	-3.26640×10^4	-1.43624×10^{10}
$Bi_2Ca_{14}Mn_{16}O_{40}$	-1.76077×10^7	1550	3032	6.27831×10^7	-3.18490×10^4	-1.20905×10^{10}

Table B.5: Thermodynamic parameters for $Bi_4Ca_{12}Mn_{16}O_{48-x}$ with varying oxygen vacancies, with formation enthalpy corrections for phase diagrams (-720 kJ/mol).

Compound	ΔH_f	S	k_0	k_1	k_2	k_3
$Bi_4Ca_{12}Mn_{16}O_{47}$	-1.80619×10^7	1374	3890	2.31037×10^8	-5.84130×10^4	-4.17530×10^{10}
$Bi_4Ca_{12}Mn_{16}O_{46}$	-1.79495×10^7	1359	3764	2.13197×10^8	-5.46320×10^4	-3.92961×10^{10}
$Bi_4Ca_{12}Mn_{16}O_{45}$	-1.78049×10^7	1396	3665	2.11203×10^8	-5.21930×10^4	-3.98614×10^{10}
$Bi_4Ca_{12}Mn_{16}O_{44}$	-1.76697×10^7	1429	3556	1.96660×10^8	-4.92040×10^4	-3.67338×10^{10}
$Bi_4Ca_{12}Mn_{16}O_{43}$	-1.74541×10^7	1420	3466	1.89570×10^8	-4.71790×10^4	-3.56390×10^{10}
$Bi_4Ca_{12}Mn_{16}O_{42}$	-1.71946×10^7	1482	3382	1.92337×10^8	-4.56030×10^4	-3.70128×10^{10}
$Bi_4Ca_{12}Mn_{16}O_{41}$	-1.69864×10^7	1455	3306	2.05483×10^8	-4.47540×10^4	-4.14804×10^{10}
$Bi_4Ca_{12}Mn_{16}O_{40}$	-1.67679×10^7	1521	3213	2.02702×10^8	-4.22820×10^4	-4.24928×10^{10}

Table B.6: Thermodynamic parameters for $Bi_6Ca_{10}Mn_{16}O_{48-x}$ with varying oxygen vacancies, with formation enthalpy corrections for phase diagrams (-720 kJ/mol).

Compound	ΔH_f	S	k_0	k_1	k_2	k_3
$Bi_6Ca_{10}Mn_{16}O_{47}$	-1.71954×10^7	1360	4036	2.68404×10^8	-6.37450×10^4	-4.79517×10^{10}
$Bi_6Ca_{10}Mn_{16}O_{46}$	-1.70540×10^7	1337	3906	2.45328×10^8	-5.97960×10^4	-4.44246×10^{10}
$Bi_6Ca_{10}Mn_{16}O_{45}$	-1.68372×10^7	1352	3762	2.11083×10^8	-5.49160×10^4	-3.80234×10^{10}
$Bi_6Ca_{10}Mn_{16}O_{44}$	-1.67316×10^7	1370	3656	1.91444×10^8	-5.18620×10^4	-3.45396×10^{10}
$Bi_6Ca_{10}Mn_{16}O_{43}$	-1.65160×10^7	1356	3566	1.74850×10^8	-4.95600×10^4	-3.12353×10^{10}
$Bi_6Ca_{10}Mn_{16}O_{42}$	-1.62849×10^7	1434	3499	1.64978×10^8	-4.81220×10^4	-2.88125×10^{10}
$Bi_6Ca_{10}Mn_{16}O_{41}$	-1.60442×10^7	1403	3460	1.67572×10^8	-4.79200×10^4	-2.94317×10^{10}
$Bi_6Ca_{10}Mn_{16}O_{40}$	-1.58210×10^7	1469	3415	1.61014×10^8	-4.70780×10^4	-2.77773×10^{10}

Table B.7: Thermodynamic parameters for $Ca_{14}Ce_2Mn_{16}O_{48-x}$ with varying oxygen vacancies, with formation enthalpy corrections for phase diagrams ($-720\,\mathrm{kJ/mol}$).

Compound	ΔH_f	S	k_0	k_1	k_2	k_3
$Ca_{14}Ce_2Mn_{16}O_{47}$	-2.04764×10^7	1522	2951	-6.22959×10^7	−20451	1.38450×10^{10}
$Ca_{14}Ce_2Mn_{16}O_{46}$	-2.03194×10^7	1522	2825	-9.24862×10^7	−16088	1.90817×10^{10}
$Ca_{14}Ce_2Mn_{16}O_{45}$	-2.01689×10^7	1555	2739	-1.08775×10^8	−13419	2.17022×10^{10}
$Ca_{14}Ce_2Mn_{16}O_{44}$	-1.99863×10^7	1606	2680	-1.12392×10^8	−12350	2.22981×10^{10}
$Ca_{14}Ce_2Mn_{16}O_{43}$	-1.97703×10^7	1606	2650	-1.10733×10^8	−11864	2.11282×10^{10}
$Ca_{14}Ce_2Mn_{16}O_{42}$	-1.95685×10^7	1603	2571	-1.32410×10^8	−10118	2.64523×10^{10}
$Ca_{14}Ce_2Mn_{16}O_{41}$	-1.93225×10^7	1616	2571	-1.23902×10^8	−11235	2.56426×10^{10}
$Ca_{14}Ce_2Mn_{16}O_{40}$	-1.90705×10^7	1639	2590	-1.03215×10^8	−13357	2.20268×10^{10}

Table B.8: Thermodynamic parameters for $Ca_{12}Ce_4Mn_{16}O_{48-x}$ with varying oxygen vacancies, with formation enthalpy corrections for phase diagrams ($-720\,\mathrm{kJ/mol}$).

Compound	ΔH_f	S	k_0	k_1	k_2	k_3
$Ca_{12}Ce_4Mn_{16}O_{47}$	-2.11659×10^7	1599	3077	-5.52009×10^7	−24086	1.47975×10^{10}
$Ca_{12}Ce_4Mn_{16}O_{46}$	-2.09809×10^7	1580	3027	-5.24886×10^7	−23369	1.35416×10^{10}
$Ca_{12}Ce_4Mn_{16}O_{45}$	-2.07499×10^7	1618	2973	-4.91282×10^7	−22609	1.23386×10^{10}
$Ca_{12}Ce_4Mn_{16}O_{44}$	-2.05471×10^7	1613	2961	-2.77653×10^7	−23587	7.64057×10^9
$Ca_{12}Ce_4Mn_{16}O_{43}$	-2.02361×10^7	1675	2888	-2.34448×10^7	−22420	6.78404×10^9
$Ca_{12}Ce_4Mn_{16}O_{42}$	-1.99959×10^7	1704	2851	7.86354×10^6	−22991	-2.30560×10^9
$Ca_{12}Ce_4Mn_{16}O_{41}$	-1.96557×10^7	1683	2764	1.00208×10^6	−20813	-2.04005×10^9
$Ca_{12}Ce_4Mn_{16}O_{40}$	-1.93592×10^7	1746	2680	-1.16313×10^7	−18362	3.69711×10^8

Table B.9: Thermodynamic parameters for $Ca_{10}Ce_6Mn_{16}O_{48-x}$ with varying oxygen vacancies, with formation enthalpy corrections for phase diagrams ($-720\,\mathrm{kJ/mol}$).

Compound	ΔH_f	S	k_0	k_1	k_2	k_3
$Ca_{10}Ce_6Mn_{16}O_{47}$	-2.18133×10^7	1662	3048	-7.66394×10^7	−21231	1.75214×10^{10}
$Ca_{10}Ce_6Mn_{16}O_{46}$	-2.15791×10^7	1667	2854	-1.43770×10^8	−13788	3.13418×10^{10}
$Ca_{10}Ce_6Mn_{16}O_{45}$	-2.12762×10^7	1691	2795	-1.43943×10^8	−12474	2.97846×10^{10}
$Ca_{10}Ce_6Mn_{16}O_{44}$	-2.09898×10^7	1717	2728	-1.61323×10^8	−10678	3.36763×10^{10}
$Ca_{10}Ce_6Mn_{16}O_{43}$	-2.07149×10^7	1758	2781	-1.20056×10^8	−14253	2.47711×10^{10}
$Ca_{10}Ce_6Mn_{16}O_{42}$	-2.04186×10^7	1768	2741	-1.28379×10^8	−13383	2.68098×10^{10}
$Ca_{10}Ce_6Mn_{16}O_{41}$	-2.01833×10^7	1786	2722	-1.21441×10^8	−14020	2.55745×10^{10}
$Ca_{10}Ce_6Mn_{16}O_{40}$	-1.98990×10^7	1773	2762	-8.50944×10^7	−17088	1.81016×10^{10}

Table B.10: Thermodynamic parameters for $Ca_{16}Cr_2Mn_{14}O_{48-x}$ with varying oxygen vacancies, with formation enthalpy corrections for phase diagrams ($-720\,\mathrm{kJ/mol}$).

Compound	ΔH_f	S	k_0	k_1	k_2	k_3
$Ca_{16}Cr_2Mn_{14}O_{47}$	-1.88308×10^7	1871	2820	-5.01462×10^7	−19917	1.13103×10^{10}
$Ca_{16}Cr_2Mn_{14}O_{46}$	-1.87013×10^7	1895	2771	-4.25352×10^7	−19357	9.19621×10^9
$Ca_{16}Cr_2Mn_{14}O_{45}$	-1.85568×10^7	1938	2726	-3.35148×10^7	−18961	6.78421×10^9
$Ca_{16}Cr_2Mn_{14}O_{44}$	-1.84051×10^7	1924	2682	-2.44148×10^7	−18623	4.14685×10^9
$Ca_{16}Cr_2Mn_{14}O_{43}$	-1.82422×10^7	1969	2637	-1.16164×10^7	−18299	4.31771×10^8
$Ca_{16}Cr_2Mn_{14}O_{42}$	-1.81933×10^7	2010	2576	-6.37307×10^6	−17163	-1.50660×10^9
$Ca_{16}Cr_2Mn_{14}O_{41}$	-1.79543×10^7	2040	2486	-1.66962×10^7	−14759	-2.13815×10^8
$Ca_{16}Cr_2Mn_{14}O_{40}$	-1.77562×10^7	2004	2379	-3.06435×10^7	−12292	1.88654×10^9

Table B.11: Thermodynamic parameters for $Ca_{16}Cr_4Mn_{12}O_{48-x}$ with varying oxygen vacancies, with formation enthalpy corrections for phase diagrams ($-720\,\mathrm{kJ/mol}$).

Compound	ΔH_f	S	k_0	k_1	k_2	k_3
$Ca_{16}Cr_4Mn_{12}O_{47}$	-1.79689×10^7	2323	2712	-3.58371×10^7	−18713	7.37490×10^9
$Ca_{16}Cr_4Mn_{12}O_{46}$	-1.78410×10^7	2339	2657	-2.84770×10^7	−17871	5.11722×10^9
$Ca_{16}Cr_4Mn_{12}O_{45}$	-1.76958×10^7	2364	2593	-2.75561×10^7	−16569	4.19755×10^9
$Ca_{16}Cr_4Mn_{12}O_{44}$	-1.75426×10^7	2351	2532	-2.96397×10^7	−15287	3.86070×10^9
$Ca_{16}Cr_4Mn_{12}O_{43}$	-1.74330×10^7	2418	2467	-2.98636×10^7	−14192	3.30621×10^9
$Ca_{16}Cr_4Mn_{12}O_{42}$	-1.72328×10^7	2449	2419	-2.78187×10^7	−13430	2.42415×10^9
$Ca_{16}Cr_4Mn_{12}O_{41}$	-1.70709×10^7	2441	2354	-3.03528×10^7	−12479	2.83908×10^9
$Ca_{16}Cr_4Mn_{12}O_{40}$	-1.68982×10^7	2484	2325	-1.97156×10^7	−12468	7.93374×10^7

Table B.12: Thermodynamic parameters for $Ca_{16}Cr_6Mn_{10}O_{48-x}$ with varying oxygen vacancies, with formation enthalpy corrections for phase diagrams ($-720\,\mathrm{kJ/mol}$).

Compound	ΔH_f	S	k_0	k_1	k_2	k_3
$Ca_{16}Cr_6Mn_{10}O_{47}$	-1.71048×10^7	2806	2576	-3.60524×10^7	−16198	6.43281×10^9
$Ca_{16}Cr_6Mn_{10}O_{46}$	-1.69753×10^7	2826	2517	-3.33132×10^7	−15107	5.23660×10^9
$Ca_{16}Cr_6Mn_{10}O_{45}$	-1.67935×10^7	2834	2469	-2.75611×10^7	−14465	3.48237×10^9
$Ca_{16}Cr_6Mn_{10}O_{44}$	-1.66072×10^7	2813	2422	-2.56731×10^7	−13770	2.60653×10^9
$Ca_{16}Cr_6Mn_{10}O_{43}$	-1.64991×10^7	2854	2376	-1.71797×10^7	−13583	4.30413×10^8
$Ca_{16}Cr_6Mn_{10}O_{42}$	-1.63527×10^7	2911	2327	-1.54731×10^7	−13117	1.30099×10^8
$Ca_{16}Cr_6Mn_{10}O_{41}$	-1.62156×10^7	2941	2304	-5.53072×10^5	−13707	-3.42694×10^9
$Ca_{16}Cr_6Mn_{10}O_{40}$	-1.60336×10^7	2959	2241	-1.04662×10^7	−12821	8.74002×10^6

Table B.13: Thermodynamic parameters for $Ca_{16}Cu_2Mn_{14}O_{48-x}$ with varying oxygen vacancies, with formation enthalpy corrections for phase diagrams ($-720\,\mathrm{kJ/mol}$).

Compound	ΔH_f	S	k_0	k_1	k_2	k_3
$Ca_{16}Cu_2Mn_{14}O_{47}$	-1.89800×10^7	1454	3350	8.76528×10^7	−38009	-1.65692×10^{10}
$Ca_{16}Cu_2Mn_{14}O_{46}$	-1.89895×10^7	1456	3257	8.72447×10^7	−35500	-1.78635×10^{10}
$Ca_{16}Cu_2Mn_{14}O_{45}$	-1.88569×10^7	1498	3130	5.41581×10^7	−31325	-1.10499×10^{10}
$Ca_{16}Cu_2Mn_{14}O_{44}$	-1.87260×10^7	1542	3024	3.73819×10^7	−28194	-8.27498×10^9
$Ca_{16}Cu_2Mn_{14}O_{43}$	-1.86066×10^7	1565	2899	1.77937×10^7	−24390	-5.26038×10^9
$Ca_{16}Cu_2Mn_{14}O_{42}$	-1.85060×10^7	1548	2786	3.95111×10^6	−21047	-3.37653×10^9
$Ca_{16}Cu_2Mn_{14}O_{41}$	-1.83366×10^7	1613	2599	-5.59619×10^7	−14323	8.48219×10^9
$Ca_{16}Cu_2Mn_{14}O_{40}$	-1.81777×10^7	1613	2528	-6.92977×10^7	−13256	1.24314×10^{10}

Table B.14: Thermodynamic parameters for $Ca_{16}Cu_4Mn_{12}O_{48-x}$ with varying oxygen vacancies, with formation enthalpy corrections for phase diagrams ($-720\,\mathrm{kJ/mol}$).

Compound	ΔH_f	S	k_0	k_1	k_2	k_3
$Ca_{16}Cu_4Mn_{12}O_{47}$	-1.81984×10^7	1516	3143	3.70909×10^7	−30460	-6.84431×10^9
$Ca_{16}Cu_4Mn_{12}O_{46}$	-1.81635×10^7	1520	3011	1.37283×10^6	−25850	4.30678×10^7
$Ca_{16}Cu_4Mn_{12}O_{45}$	-1.81774×10^7	1532	2838	-4.17431×10^7	−19651	7.68025×10^9
$Ca_{16}Cu_4Mn_{12}O_{44}$	-1.81684×10^7	1529	2757	-3.34137×10^7	−17818	4.38414×10^9
$Ca_{16}Cu_4Mn_{12}O_{43}$	-1.80308×10^7	1548	2647	-7.32047×10^7	−14251	1.31981×10^{10}
$Ca_{16}Cu_4Mn_{12}O_{42}$	-1.78650×10^7	1573	2622	-6.64695×10^7	−14632	1.22073×10^{10}
$Ca_{16}Cu_4Mn_{12}O_{41}$	-1.76704×10^7	1615	2565	-6.18270×10^7	−14163	1.11493×10^{10}
$Ca_{16}Cu_4Mn_{12}O_{40}$	-1.75847×10^7	1633	2488	-6.76117×10^7	−12316	1.20137×10^{10}

Table B.15: Thermodynamic parameters for $Ca_{16}Cu_6Mn_{10}O_{48-x}$ with varying oxygen vacancies, with formation enthalpy corrections for phase diagrams ($-720\,\mathrm{kJ/mol}$).

Compound	ΔH_f	S	k_0	k_1	k_2	k_3
$Ca_{16}Cu_6Mn_{10}O_{47}$	-1.74092×10^7	1579	2911	-3.33111×10^7	−21111	6.80348×10^9
$Ca_{16}Cu_6Mn_{10}O_{46}$	-1.74597×10^7	1571	2893	-3.16159×10^7	−21251	6.31991×10^9
$Ca_{16}Cu_6Mn_{10}O_{45}$	-1.73792×10^7	1585	2850	-3.57986×10^7	−20504	7.11576×10^9
$Ca_{16}Cu_6Mn_{10}O_{44}$	-1.73273×10^7	1594	2810	-3.30081×10^7	−20269	6.57309×10^9
$Ca_{16}Cu_6Mn_{10}O_{43}$	-1.73229×10^7	1620	2730	-5.52083×10^7	−17599	1.11636×10^{10}
$Ca_{16}Cu_6Mn_{10}O_{42}$	-1.71742×10^7	1636	2578	-9.40652×10^7	−12378	1.86358×10^{10}
$Ca_{16}Cu_6Mn_{10}O_{41}$	-1.70677×10^7	1655	2662	-4.08985×10^7	−17502	8.09359×10^9
$Ca_{16}Cu_6Mn_{10}O_{40}$	-1.70079×10^7	1689	2541	-5.74373×10^7	−14246	1.08707×10^{10}

Table B.16: Thermodynamic parameters for $Ca_{16}Fe_4Mn_{12}O_{48-x}$ with varying oxygen vacancies, with formation enthalpy corrections for phase diagrams ($-720\,\mathrm{kJ/mol}$).

Compound	ΔH_f	S	k_0	k_1	k_2	k_3
$Ca_{16}Fe_4Mn_{12}O_{47}$	-1.95743×10^7	1418	2491	-1.48167×10^8	-4198	2.52050×10^{10}
$Ca_{16}Fe_4Mn_{12}O_{46}$	-1.94406×10^7	1454	2400	-1.56823×10^8	-1867	2.65536×10^{10}
$Ca_{16}Fe_4Mn_{12}O_{45}$	-1.93124×10^7	1486	2303	-1.67610×10^8	688	2.82726×10^{10}
$Ca_{16}Fe_4Mn_{12}O_{44}$	-1.91398×10^7	1513	2203	-1.78592×10^8	3301	2.99253×10^{10}
$Ca_{16}Fe_4Mn_{12}O_{43}$	-1.90123×10^7	1531	2091	-1.87558×10^8	5907	3.09469×10^{10}
$Ca_{16}Fe_4Mn_{12}O_{42}$	-1.87966×10^7	1565	1997	-1.97875×10^8	8610	3.23016×10^{10}
$Ca_{16}Fe_4Mn_{12}O_{41}$	-1.86305×10^7	1572	1891	-2.05961×10^8	11031	3.30401×10^{10}
$Ca_{16}Fe_4Mn_{12}O_{40}$	-1.83261×10^7	1594	1815	-2.13866×10^8	13419	3.37333×10^{10}

Table B.17: Thermodynamic parameters for $Ca_{16}Fe_6Mn_{10}O_{48-x}$ with varying oxygen vacancies, with formation enthalpy corrections for phase diagrams ($-720\,\mathrm{kJ/mol}$).

Compound	ΔH_f	S	k_0	k_1	k_2	k_3
$Ca_{16}Fe_6Mn_{10}O_{47}$	-1.94951×10^7	1426	1966	-2.94384×10^8	16899	5.10845×10^{10}
$Ca_{16}Fe_6Mn_{10}O_{46}$	-1.94161×10^7	1475	1847	-3.17806×10^8	20653	5.52880×10^{10}
$Ca_{16}Fe_6Mn_{10}O_{45}$	-1.93165×10^7	1485	1741	-3.39421×10^8	23952	5.93258×10^{10}
$Ca_{16}Fe_6Mn_{10}O_{44}$	-1.91798×10^7	1492	1641	-3.57679×10^8	26571	6.27244×10^{10}
$Ca_{16}Fe_6Mn_{10}O_{43}$	-1.90788×10^7	1498	1554	-3.75160×10^8	29216	6.60943×10^{10}
$Ca_{16}Fe_6Mn_{10}O_{42}$	-1.89003×10^7	1515	1468	-3.88816×10^8	31309	6.86490×10^{10}
$Ca_{16}Fe_6Mn_{10}O_{41}$	-1.87636×10^7	1516	1396	-4.00813×10^8	33069	7.09459×10^{10}
$Ca_{16}Fe_6Mn_{10}O_{40}$	-1.83741×10^7	1743	1332	-4.10273×10^8	34882	7.26199×10^{10}

Table B.18: Thermodynamic parameters for $Ca_{14}La_2Mn_{16}O_{48-x}$ with varying oxygen vacancies, with formation enthalpy corrections for phase diagrams ($-720\,\mathrm{kJ/mol}$).

Compound	ΔH_f	S	k_0	k_1	k_2	k_3
$Ca_{14}La_2Mn_{16}O_{47}$	-2.01280×10^7	1423	2851	-1.02404×10^8	-16900	2.29548×10^{10}
$Ca_{14}La_2Mn_{16}O_{46}$	-1.99991×10^7	1438	2774	-1.29548×10^8	-14171	2.86777×10^{10}
$Ca_{14}La_2Mn_{16}O_{45}$	-1.98361×10^7	1458	2767	-1.19387×10^8	-14680	2.61087×10^{10}
$Ca_{14}La_2Mn_{16}O_{44}$	-1.96795×10^7	1478	2723	-1.36168×10^8	-13824	3.06186×10^{10}
$Ca_{14}La_2Mn_{16}O_{43}$	-1.94870×10^7	1495	2775	-1.01607×10^8	-17508	2.38955×10^{10}
$Ca_{14}La_2Mn_{16}O_{42}$	-1.93006×10^7	1495	2818	-5.36163×10^7	-21065	1.32231×10^{10}
$Ca_{14}La_2Mn_{16}O_{41}$	-1.90994×10^7	1550	2854	-5.21024×10^6	-24272	2.39965×10^9
$Ca_{14}La_2Mn_{16}O_{40}$	-1.88482×10^7	1555	2846	2.23382×10^7	-25695	-3.42872×10^9

Table B.19: Thermodynamic parameters for $Ca_{12}La_4Mn_{16}O_{48-x}$ with varying oxygen vacancies, with formation enthalpy corrections for phase diagrams ($-720\,\mathrm{kJ/mol}$).

Compound	ΔH_f	S	k_0	k_1	k_2	k_3
$Ca_{12}La_4Mn_{16}O_{47}$	-2.05954×10^7	1402	2974	-5.69180×10^7	−22562	1.56622×10^{10}
$Ca_{12}La_4Mn_{16}O_{46}$	-2.04585×10^7	1423	2941	-4.15502×10^7	−22812	1.23369×10^{10}
$Ca_{12}La_4Mn_{16}O_{45}$	-2.02513×10^7	1415	2901	-2.86741×10^7	−23037	9.64480×10^9
$Ca_{12}La_4Mn_{16}O_{44}$	-2.00496×10^7	1440	2856	-2.21559×10^7	−22799	8.22282×10^9
$Ca_{12}La_4Mn_{16}O_{43}$	-1.98466×10^7	1441	2801	-1.34365×10^7	−22535	5.90165×10^9
$Ca_{12}La_4Mn_{16}O_{42}$	-1.96220×10^7	1421	2745	-5.05267×10^6	−22453	3.24266×10^9
$Ca_{12}La_4Mn_{16}O_{41}$	-1.93804×10^7	1476	2713	3.44473×10^6	−22315	8.17072×10^8
$Ca_{12}La_4Mn_{16}O_{40}$	-1.91025×10^7	1500	2673	7.13586×10^6	−21825	-2.90137×10^8

Table B.20: Thermodynamic parameters for $Ca_{10}La_6Mn_{16}O_{48-x}$ with varying oxygen vacancies, with formation enthalpy corrections for phase diagrams ($-720\,\mathrm{kJ/mol}$).

Compound	ΔH_f	S	k_0	k_1	k_2	k_3
$Ca_{10}La_6Mn_{16}O_{47}$	-2.10288×10^7	1343	2965	-7.01808×10^7	−21704	1.85315×10^{10}
$Ca_{10}La_6Mn_{16}O_{46}$	-2.08406×10^7	1392	2913	-5.55219×10^7	−21335	1.45539×10^{10}
$Ca_{10}La_6Mn_{16}O_{45}$	-2.06990×10^7	1390	2877	-3.92658×10^7	−21350	1.05287×10^{10}
$Ca_{10}La_6Mn_{16}O_{44}$	-2.05272×10^7	1381	2834	-3.34559×10^7	−20850	9.30290×10^9
$Ca_{10}La_6Mn_{16}O_{43}$	-2.02512×10^7	1371	2783	-2.32614×10^7	−20724	5.99505×10^9
$Ca_{10}La_6Mn_{16}O_{42}$	-1.99559×10^7	1346	2715	-2.75048×10^7	−19698	6.14132×10^9
$Ca_{10}La_6Mn_{16}O_{41}$	-1.97156×10^7	1412	2663	-2.83149×10^7	−18720	6.34414×10^9
$Ca_{10}La_6Mn_{16}O_{40}$	-1.94815×10^7	1432	2627	-2.50911×10^7	−18263	5.35794×10^9

Table B.21: Thermodynamic parameters for $Ca_{16}Mg_2Mn_{14}O_{48-x}$ with varying oxygen vacancies, with formation enthalpy corrections for phase diagrams ($-720\,\mathrm{kJ/mol}$).

Compound	ΔH_f	S	k_0	k_1	k_2	k_3
$Ca_{16}Mg_2Mn_{14}O_{47}$	-1.99089×10^7	1585	2861	-4.84112×10^7	−20058	9.83224×10^9
$Ca_{16}Mg_2Mn_{14}O_{46}$	-1.98220×10^7	1600	2809	-3.23138×10^7	−19472	5.19680×10^9
$Ca_{16}Mg_2Mn_{14}O_{45}$	-1.96861×10^7	1634	2785	-2.77386×10^6	−20243	-1.86803×10^9
$Ca_{16}Mg_2Mn_{14}O_{44}$	-1.95355×10^7	1657	2746	8.69404×10^6	−20090	-3.84142×10^9
$Ca_{16}Mg_2Mn_{14}O_{43}$	-1.94180×10^7	1719	2694	1.40542×10^7	−19392	-6.06263×10^9
$Ca_{16}Mg_2Mn_{14}O_{42}$	-1.92956×10^7	1685	2632	8.46093×10^6	−18189	-5.00956×10^9
$Ca_{16}Mg_2Mn_{14}O_{41}$	-1.90777×10^7	1758	2567	6.51895×10^6	−17440	-4.32155×10^9
$Ca_{16}Mg_2Mn_{14}O_{40}$	-1.89379×10^7	1775	2516	2.23364×10^6	−16734	-3.29071×10^9

Table B.22: Thermodynamic parameters for $Ca_{16}Mg_4Mn_{12}O_{48-x}$ with varying oxygen vacancies, with formation enthalpy corrections for phase diagrams ($-720\,\mathrm{kJ/mol}$).

Compound	ΔH_f	S	k_0	k_1	k_2	k_3
$Ca_{16}Mg_4Mn_{12}O_{47}$	-2.00209×10^7	1800	2840	-1.71698×10^7	-21134	2.77892×10^9
$Ca_{16}Mg_4Mn_{12}O_{46}$	-1.99925×10^7	1821	2793	-7.56109×10^6	-20752	1.68690×10^8
$Ca_{16}Mg_4Mn_{12}O_{45}$	-1.99309×10^7	1835	2743	-7.34354×10^5	-20134	-1.94918×10^9
$Ca_{16}Mg_4Mn_{12}O_{44}$	-1.98558×10^7	1841	2686	4.82984×10^6	-19359	-3.78151×10^9
$Ca_{16}Mg_4Mn_{12}O_{43}$	-1.97040×10^7	1868	2620	6.94910×10^6	-18241	-4.93561×10^9
$Ca_{16}Mg_4Mn_{12}O_{42}$	-1.96217×10^7	1867	2547	7.10486×10^6	-16873	-5.59268×10^9
$Ca_{16}Mg_4Mn_{12}O_{41}$	-1.94301×10^7	1906	2473	2.92868×10^5	-14896	-4.98002×10^9
$Ca_{16}Mg_4Mn_{12}O_{40}$	-1.93344×10^7	1927	2395	-7.12702×10^6	-12558	-4.15538×10^9

Table B.23: Thermodynamic parameters for $Ca_{16}Mg_6Mn_{10}O_{48-x}$ with varying oxygen vacancies, with formation enthalpy corrections for phase diagrams ($-720\,\mathrm{kJ/mol}$).

Compound	ΔH_f	S	k_0	k_1	k_2	k_3
$Ca_{16}Mg_6Mn_{10}O_{47}$	-2.00599×10^7	2026	2788	1.68957×10^6	-20709	-2.02588×10^9
$Ca_{16}Mg_6Mn_{10}O_{46}$	-2.00738×10^7	2034	2737	7.55704×10^6	-20457	-3.75207×10^9
$Ca_{16}Mg_6Mn_{10}O_{45}$	-2.00864×10^7	2051	2691	1.36158×10^7	-20096	-5.49879×10^9
$Ca_{16}Mg_6Mn_{10}O_{44}$	-1.99176×10^7	2064	2642	2.35808×10^7	-19687	-7.99389×10^9
$Ca_{16}Mg_6Mn_{10}O_{43}$	-1.99089×10^7	2091	2592	2.75809×10^7	-19104	-9.25916×10^9
$Ca_{16}Mg_6Mn_{10}O_{42}$	-1.98371×10^7	2083	2552	3.36489×10^7	-18755	-1.11176×10^{10}
$Ca_{16}Mg_6Mn_{10}O_{41}$	-1.97836×10^7	2092	2500	3.56851×10^7	-18000	-1.18590×10^{10}
$Ca_{16}Mg_6Mn_{10}O_{40}$	-1.96464×10^7	2085	2455	4.18783×10^7	-17736	-1.33988×10^{10}

Table B.24: Thermodynamic parameters for $Ca_{16}Mn_{14}Mo_2O_{48-x}$ with varying oxygen vacancies, with formation enthalpy corrections for phase diagrams ($-720\,\mathrm{kJ/mol}$).

Compound	ΔH_f	S	k_0	k_1	k_2	k_3
$Ca_{16}Mn_{14}Mo_2O_{47}$	-2.01756×10^7	1437	3097	2.26806×10^7	-28832	-3.86389×10^9
$Ca_{16}Mn_{14}Mo_2O_{46}$	-1.99961×10^7	1499	3006	1.60133×10^7	-26414	-3.54576×10^9
$Ca_{16}Mn_{14}Mo_2O_{45}$	-1.98384×10^7	1482	2910	3.77616×10^6	-24031	-1.67282×10^9
$Ca_{16}Mn_{14}Mo_2O_{44}$	-1.96645×10^7	1479	2832	-6.90640×10^6	-22140	2.17501×10^7
$Ca_{16}Mn_{14}Mo_2O_{43}$	-1.94128×10^7	1516	2768	-9.90096×10^6	-20927	4.00448×10^8
$Ca_{16}Mn_{14}Mo_2O_{42}$	-1.91629×10^7	1546	2720	-1.01091×10^7	-20129	2.37543×10^8
$Ca_{16}Mn_{14}Mo_2O_{41}$	-1.90106×10^7	1567	2678	-1.05502×10^7	-19339	1.48824×10^8
$Ca_{16}Mn_{14}Mo_2O_{40}$	-1.87437×10^7	1600	2655	-6.35580×10^6	-19026	-1.29121×10^9

Table B.25: Thermodynamic parameters for $Ca_{16}Mn_{12}Mo_4O_{48-x}$ with varying oxygen vacancies, with formation enthalpy corrections for phase diagrams ($-720\,\mathrm{kJ/mol}$).

Compound	ΔH_f	S	k_0	k_1	k_2	k_3
$Ca_{16}Mn_{12}Mo_4O_{47}$	-2.06016×10^7	1405	3211	6.80745×10^7	−34427	-1.38043×10^{10}
$Ca_{16}Mn_{12}Mo_4O_{46}$	-2.04115×10^7	1426	3160	7.41006×10^7	−33640	-1.57575×10^{10}
$Ca_{16}Mn_{12}Mo_4O_{45}$	-2.01746×10^7	1454	3110	8.35667×10^7	−33005	-1.81218×10^{10}
$Ca_{16}Mn_{12}Mo_4O_{44}$	-1.99216×10^7	1443	3045	8.97033×10^7	−32413	-1.98935×10^{10}
$Ca_{16}Mn_{12}Mo_4O_{43}$	-1.96372×10^7	1475	3002	9.90526×10^7	−31948	-2.20969×10^{10}
$Ca_{16}Mn_{12}Mo_4O_{42}$	-1.93573×10^7	1532	2956	1.06937×10^8	−31408	-2.39593×10^{10}
$Ca_{16}Mn_{12}Mo_4O_{41}$	-1.90675×10^7	1535	2902	1.09405×10^8	−30678	-2.48788×10^{10}
$Ca_{16}Mn_{12}Mo_4O_{40}$	-1.87582×10^7	1602	2862	1.12813×10^8	−29865	-2.58520×10^{10}

Table B.26: Thermodynamic parameters for $Ca_{16}Mn_{10}Mo_6O_{48-x}$ with varying oxygen vacancies, with formation enthalpy corrections for phase diagrams ($-720\,\mathrm{kJ/mol}$).

Compound	ΔH_f	S	k_0	k_1	k_2	k_3
$Ca_{16}Mn_{10}Mo_6O_{47}$	-2.09341×10^7	1386	3386	1.35571×10^8	−42385	-2.76410×10^{10}
$Ca_{16}Mn_{10}Mo_6O_{46}$	-2.06286×10^7	1466	3404	1.45117×10^8	−42798	-2.94544×10^{10}
$Ca_{16}Mn_{10}Mo_6O_{45}$	-2.03565×10^7	1460	3354	1.47946×10^8	−42745	-3.00749×10^{10}
$Ca_{16}Mn_{10}Mo_6O_{44}$	-2.00803×10^7	1493	3343	1.48025×10^8	−42254	-3.03162×10^{10}
$Ca_{16}Mn_{10}Mo_6O_{43}$	-1.98155×10^7	1480	3256	1.49191×10^8	−41484	-3.09207×10^{10}
$Ca_{16}Mn_{10}Mo_6O_{42}$	-1.95031×10^7	1496	3233	1.58499×10^8	−41217	-3.38686×10^{10}
$Ca_{16}Mn_{10}Mo_6O_{41}$	-1.91686×10^7	1533	3248	1.98039×10^8	−43598	-4.29504×10^{10}
$Ca_{16}Mn_{10}Mo_6O_{40}$	-1.88120×10^7	1544	3253	2.20973×10^8	−45304	-4.71844×10^{10}

Table B.27: Thermodynamic parameters for $Ca_{14}Mn_{16}O_{48-x}Sr_2$ with varying oxygen vacancies, with formation enthalpy corrections for phase diagrams ($-720\,\mathrm{kJ/mol}$).

Compound	ΔH_f	S	k_0	k_1	k_2	k_3
$Ca_{14}Mn_{16}O_{47}Sr_2$	-1.96294×10^7	1472	2933	-9.26732×10^7	−19767	2.22612×10^{10}
$Ca_{14}Mn_{16}O_{46}Sr_2$	-1.95147×10^7	1513	2985	-7.54993×10^7	−22331	1.93786×10^{10}
$Ca_{14}Mn_{16}O_{45}Sr_2$	-1.93832×10^7	1530	3029	-5.67259×10^7	−24813	1.59672×10^{10}
$Ca_{14}Mn_{16}O_{44}Sr_2$	-1.92753×10^7	1554	3093	-8.63167×10^6	−29049	5.39763×10^9
$Ca_{14}Mn_{16}O_{43}Sr_2$	-1.90816×10^7	1573	3201	5.38456×10^7	−35489	-6.98478×10^9
$Ca_{14}Mn_{16}O_{42}Sr_2$	-1.89547×10^7	1592	3174	7.91129×10^7	−36180	-1.30042×10^{10}
$Ca_{14}Mn_{16}O_{41}Sr_2$	-1.87572×10^7	1641	3070	7.55749×10^7	−33920	-1.30228×10^{10}
$Ca_{14}Mn_{16}O_{40}Sr_2$	-1.85150×10^7	1615	2950	5.91855×10^7	−30467	-1.05602×10^{10}

Table B.28: Thermodynamic parameters for $Ca_{12}Mn_{16}O_{48-x}Sr_4$ with varying oxygen vacancies, with formation enthalpy corrections for phase diagrams ($-720\,\mathrm{kJ/mol}$).

Compound	ΔH_f	S	k_0	k_1	k_2	k_3
$Ca_{12}Mn_{16}O_{47}Sr_4$	-1.95920×10^7	1518	3034	-2.59649×10^7	−25214	8.33776×10^9
$Ca_{12}Mn_{16}O_{46}Sr_4$	-1.94599×10^7	1562	2977	-1.46134×10^7	−24401	4.92646×10^9
$Ca_{12}Mn_{16}O_{45}Sr_4$	-1.93473×10^7	1577	2889	-1.76896×10^7	−22334	4.45057×10^9
$Ca_{12}Mn_{16}O_{44}Sr_4$	-1.92020×10^7	1609	2804	-2.84494×10^7	−19781	5.63707×10^9
$Ca_{12}Mn_{16}O_{43}Sr_4$	-1.90493×10^7	1612	2710	-4.46621×10^7	−17197	8.53512×10^9
$Ca_{12}Mn_{16}O_{42}Sr_4$	-1.89528×10^7	1594	2640	-5.86573×10^7	−15055	1.07219×10^{10}
$Ca_{12}Mn_{16}O_{41}Sr_4$	-1.86993×10^7	1642	2552	-6.84302×10^7	−13182	1.25995×10^{10}
$Ca_{12}Mn_{16}O_{40}Sr_4$	-1.84995×10^7	1643	2509	-6.92053×10^7	−12560	1.24022×10^{10}

Table B.29: Thermodynamic parameters for $Ca_{10}Mn_{16}O_{48-x}Sr_6$ with varying oxygen vacancies, with formation enthalpy corrections for phase diagrams ($-720\,\mathrm{kJ/mol}$).

Compound	ΔH_f	S	k_0	k_1	k_2	k_3
$Ca_{10}Mn_{16}O_{47}Sr_6$	-1.95710×10^7	1553	3007	-3.56541×10^7	−23534	9.33802×10^9
$Ca_{10}Mn_{16}O_{46}Sr_6$	-1.94525×10^7	1571	2923	-4.63892×10^7	−21102	1.07541×10^{10}
$Ca_{10}Mn_{16}O_{45}Sr_6$	-1.93260×10^7	1627	2847	-6.75759×10^7	−18941	1.59760×10^{10}
$Ca_{10}Mn_{16}O_{44}Sr_6$	-1.91710×10^7	1666	2869	-3.93827×10^7	−21257	1.00955×10^{10}
$Ca_{10}Mn_{16}O_{43}Sr_6$	-1.90002×10^7	1646	2898	-1.98377×10^6	−23947	1.40622×10^9
$Ca_{10}Mn_{16}O_{42}Sr_6$	-1.88554×10^7	1661	2886	1.92866×10^7	−25006	-3.60472×10^9
$Ca_{10}Mn_{16}O_{41}Sr_6$	-1.86194×10^7	1695	2876	4.67241×10^7	−26548	-9.59111×10^9
$Ca_{10}Mn_{16}O_{40}Sr_6$	-1.84771×10^7	1689	2846	5.85324×10^7	−26802	-1.21372×10^{10}

Table B.30: Thermodynamic parameters for $Ca_{16}Mn_{14}O_{48-x}Ti_2$ with varying oxygen vacancies, with formation enthalpy corrections for phase diagrams ($-720\,\mathrm{kJ/mol}$).

Compound	ΔH_f	S	k_0	k_1	k_2	k_3
$Ca_{16}Mn_{14}O_{47}Ti_2$	-2.06443×10^7	1459	2890	-3.85645×10^7	−20686	7.98156×10^9
$Ca_{16}Mn_{14}O_{46}Ti_2$	-2.05163×10^7	1475	2843	-3.58460×10^7	−19861	6.88095×10^9
$Ca_{16}Mn_{14}O_{45}Ti_2$	-2.03584×10^7	1502	2805	-3.42531×10^7	−19374	6.18314×10^9
$Ca_{16}Mn_{14}O_{44}Ti_2$	-2.01831×10^7	1494	2775	-3.02685×10^7	−19153	4.98458×10^9
$Ca_{16}Mn_{14}O_{43}Ti_2$	-2.00444×10^7	1527	2728	-2.66412×10^7	−18424	3.12212×10^9
$Ca_{16}Mn_{14}O_{42}Ti_2$	-1.99047×10^7	1578	2662	-2.22376×10^7	−17259	4.61772×10^8
$Ca_{16}Mn_{14}O_{41}Ti_2$	-1.96685×10^7	1532	2577	-6.60479×10^7	−14345	1.13326×10^{10}
$Ca_{16}Mn_{14}O_{40}Ti_2$	-1.93730×10^7	1583	2587	-6.56717×10^7	−15290	1.27892×10^{10}

Table B.31: Thermodynamic parameters for $Ca_{16}Mn_{12}O_{48-x}Ti_4$ with varying oxygen vacancies, with formation enthalpy corrections for phase diagrams ($-720\,\mathrm{kJ/mol}$).

Compound	ΔH_f	S	k_0	k_1	k_2	k_3
$Ca_{16}Mn_{12}O_{47}Ti_4$	-2.15972×10^7	1482	2826	-3.62464×10^7	−19194	6.33490×10^9
$Ca_{16}Mn_{12}O_{46}Ti_4$	-2.14463×10^7	1484	2779	-2.88871×10^7	−18737	4.29385×10^9
$Ca_{16}Mn_{12}O_{45}Ti_4$	-2.12529×10^7	1542	2730	-2.06208×10^7	−18306	2.01213×10^9
$Ca_{16}Mn_{12}O_{44}Ti_4$	-2.11384×10^7	1587	2671	-1.09130×10^7	−17924	-6.21050×10^8
$Ca_{16}Mn_{12}O_{43}Ti_4$	-2.09121×10^7	1587	2623	6.88620×10^5	−17709	-3.78076×10^9
$Ca_{16}Mn_{12}O_{42}Ti_4$	-2.06817×10^7	1635	2575	1.47155×10^7	−17564	-7.34386×10^9
$Ca_{16}Mn_{12}O_{41}Ti_4$	-2.05801×10^7	1664	2542	3.04273×10^7	−17660	-1.13371×10^{10}
$Ca_{16}Mn_{12}O_{40}Ti_4$	-1.95131×10^7	1659	2492	4.86032×10^7	−18022	-1.59378×10^{10}

Table B.32: Thermodynamic parameters for $Ca_{16}Mn_{10}O_{48-x}Ti_6$ with varying oxygen vacancies, with formation enthalpy corrections for phase diagrams ($-720\,\mathrm{kJ/mol}$).

Compound	ΔH_f	S	k_0	k_1	k_2	k_3
$Ca_{16}Mn_{10}O_{47}Ti_6$	-2.25562×10^7	1508	2775	-2.19469×10^7	−18394	1.94949×10^9
$Ca_{16}Mn_{10}O_{46}Ti_6$	-2.24086×10^7	1659	2736	-9.24137×10^6	−18424	-9.59410×10^8
$Ca_{16}Mn_{10}O_{45}Ti_6$	-2.22303×10^7	1560	2688	2.87284×10^6	−18375	-3.84374×10^9
$Ca_{16}Mn_{10}O_{44}Ti_6$	-2.20165×10^7	1576	2640	1.47529×10^7	−18266	-6.91316×10^9
$Ca_{16}Mn_{10}O_{43}Ti_6$	-2.17938×10^7	1674	2582	2.37292×10^7	−17917	-9.31356×10^9
$Ca_{16}Mn_{10}O_{42}Ti_6$	-2.15720×10^7	1631	2531	3.32530×10^7	−17381	-1.17736×10^{10}
$Ca_{16}Mn_{10}O_{41}Ti_6$	-2.13500×10^7	1669	2494	4.03527×10^7	−16827	-1.38915×10^{10}
$Ca_{16}Mn_{10}O_{40}Ti_6$	-2.10546×10^7	1701	2426	4.44691×10^7	−15910	-1.52516×10^{10}

DEPARTMENT OF SPACE, EARTH AND ENVIRONMENT
CHALMERS UNIVERSITY OF TECHNOLOGY
Gothenburg, Sweden
www.chalmers.se

CHALMERS
UNIVERSITY OF TECHNOLOGY